Petroleum Science 23 (2026) 4891–4913

Contents lists available at ScienceDirect

Petroleum Science

journal homepage: www.keaipublishing.com/en/journals/petroleum-science

Original Paper

The influence of energy enhancement on the morphology of hydraulic fractures based on a fully-coupled XFEM method

Pin-Jin Zhang [a], Yun Zhou [a,*], Shan-Po Jia [a], Zong-Feng Zhang [b], Bin-Tao Wang [c], Dian-Sen Yang [d]

[a] Bohai Rim Energy Research Institute, Northeast Petroleum University, Qinhuangdao, 066004, Hebei, China
[b] Sinopec Shanghai Offshore Oil Bureau Co. Ltd., Shanghai, 200120, China
[c] Daqing Oilfield Co., Ltd., PetroChina Company Limited, Daqing, 163453, Heilongjiang, China
[d] School of Civil Engineering, Wuhan University, Wuhan, 430072, Hubei, China

A R T I C L E I N F O

Article history:
Received 10 June 2025
Received in revised form
20 January 2026
Accepted 2 June 2026
Available online 9 June 2026

Edited by Xi Zhang

Keywords:
Hydraulic fracturing
Energy enhancement
XFEM
Hydro-mechanical coupling
Fracture morphology
Poroelastic response

A B S T R A C T

Pre-fracturing energy enhancement has shown promising potential to improve stimulation performance in low-permeability reservoirs, yet its influence on subsequent hydraulic fracturing remains unclear. This study develops a fully coupled hydro-mechanical model based on the XFEM to simulate this integrated process. Both displacement and pressure fields are discretized using XFEM with appropriate enrichment functions, enabling accurate representation of fracture-induced discontinuities. A unified computational framework is established to solve the coupled hydro-mechanical response during two sequential stages: energy-enhanced injection and hydraulic fracturing. The model accuracy is validated against the classical KGD problem in permeable media. Numerical analyses are conducted to investigate stress redistribution and pore pressure evolution during energy enhancement. Parametric studies are performed to quantify the influence of injection volume, injection rate, matrix permeability, shut-in time, and fracture initiation location on fracture propagation behavior. Results show that energy enhancement elevates pore pressure and total stress, thereby reducing fluid leak-off and enhancing fracturing efficiency, though at the cost of higher injection pressure. Specifically, in a 1 mD reservoir, 30-day energy enhancement via water injection at a rate of 2.61 $m^3/(m \cdot day)$ raises fracture propagation pressure by over 5.63 MPa compared to the non-enhanced case, while fracturing efficiency improves from 51.09% to 80.5%, and fracture length increases from 24.7 m to 50.0 m under a stimulation time of 40 s. Fracture initiation location significantly influences fracture propagation path, aperture, and symmetry. Initiating a fracture 10 m away along the minimum stress direction results in a symmetric but deflected path, with a maximum tip deviation of 3.96 m at a 50 m fracture length. In contrast, initiation along the maximum stress direction results in severely asymmetric propagation. The growth of one wing is strongly suppressed, extending only about 5 m when the total fracture length is 50 m. These findings provide critical insights for optimizing energy-enhanced fracturing treatments in unconventional reservoirs.

1. Introduction

Low-permeability reservoirs typically exhibit limited fluid mobility, making effective stimulation techniques essential for economic development. Hydraulic fracturing has emerged as a critical method for improving reservoir performance by connecting natural fractures and generating complex fracture networks, thereby increasing permeability and production potential (Ji and Fang, 2023). The resulting fracture geometry and complexity play a central role in determining stimulation effectiveness and long-term hydrocarbon recovery (Yuan et al., 2015; Hu et al., 2024). In recent years, a modified strategy involving the injection of fluids (e.g., H_2O, CO_2, N_2, or surfactants) before conventional hydraulic fracturing has been proposed for low-permeability, low-pressure reservoirs like China's Daqing Oilfield. Field trials demonstrate that this pre-fracturing energy enhancement (EE) treatment significantly improves oil and gas

* Corresponding author.
E-mail address: nepu_zhouyun@163.com (Y. Zhou).
Peer review under the responsibility of China University of Petroleum (Beijing).

https://doi.org/10.1016/j.petsci.2026.06.004

production compared to fracturing alone. The enhancement mechanism operates through two primary effects: the injected fluid increases reservoir pressure to promote flow, while simultaneously reducing crude oil viscosity and enhancing displacement efficiency, thereby improving recovery. However, this EE process inevitably alters the reservoir's pressure and stress distribution, potentially influencing subsequent hydraulic fracture (HF) propagation. Understanding these interactions is crucial for optimizing integrated EE-fracturing treatment design.

Theoretical analyses and field observations both confirm that pore pressure gradients from injection or production disturb the initial stress field, creating non-uniform stress distributions and altering principal stress directions (Atefi-Monfared and Rybicki, 2018; Zhu et al., 2021; Ma et al., 2023). Using Biot's poroelastic theory, Detournay and Cheng (1988) developed analytical solutions for stress, displacement, and pore pressure around a wellbore under constant wellbore pressure. Their work was extended by Siebrits et al. (2000), who introduced the concept of a stress reversal zone and examined its extent through 3D numerical simulations. Recent studies revealed that both the extent of stress reorientation and the size of the reversal zone depend on multiple factors, including the initial stress contrast, formation permeability, fluid viscosity, injection/production rates, and production duration (Li, 2024; Deng et al., 2024; Wang et al., 2024; Wang et al., 2025). Stress redistribution has been shown to cause fracture reorientation, as evidenced by laboratory experiments (AlTammar et al., 2018; Lu et al., 2020), field measurements (Wang et al., 2022; Ma et al., 2024; Wei et al., 2025), and numerical modeling (Zhang et al., 2022). For example, AlTammar et al. (2018) used digital image correlation to explore fracture interactions and pressure evolution in porous media exposed to multiple injection points and anisotropic far-field stresses. Field monitoring results from the Changqing Oilfield show that during refracturing, fractures tend to propagate preferentially into depleted zones (Wang et al., 2022). However, laboratory experiments are limited by scale effects, and hydro-mechanical coupling complicates the detection of fracture reorientation in the field (You et al., 2025). These challenges make numerical simulation an increasingly vital tool for investigating HF behavior under evolving pore pressure conditions.

Numerical investigations into how injection and production influence fracture propagation have been ongoing for decades. Early studies primarily predicted fracture propagation based solely on stress orientation analyses (Gupta et al., 2012; Atefi-Monfared and Rybicki, 2018). Subsequent research incorporated poroelastic coupling to simulate fracture deviation induced by depletion-driven stress reorientation. To this end, the finite difference method (FDM) was coupled with the boundary element method (BEM) or the discrete element method (DEM) to capture the interactions between fluid flow and rock deformation (Safari et al., 2017; Zhang et al., 2022). Despite their effectiveness, FDM-based approaches tend to be less flexible when simulating complex reservoir geometries and strongly coupled hydro-mechanical processes. In contrast, finite element methods (FEM), owing to their generality and versatility, provide a more flexible framework for simulating poroelastic responses. Guo et al. (2019) used a coupled FEM–BEM framework to examine how parent-well production alters stress and pore pressure fields, thereby affecting infill-well fracture behavior. To avoid the complexities associated with transferring nodal quantities between different numerical methods, FEM-based damage models have simulated poroelastic variations and fracture propagation within unified frameworks (Wang et al., 2013; Li et al., 2017). These studies show that both pore pressure and in-situ stress ratios govern fracture behavior and help identify optimal refracturing windows. FEM with cohesive elements has also been employed to simulate injection-induced fracture propagation and natural fracture interactions (Dong et al., 2023; Li et al., 2025). However, standard FEM struggles to model arbitrary fracture paths, prompting adoption of the extended finite element method (XFEM). Zhou et al. (2015) modeled the hydro-mechanical coupled production process using another simulator, and investigated refracturing operations after one year of production using XFEM. Gao et al. (2019) leveraged ABAQUS-based XFEM to investigate fracture propagation near production and injection wells. Wang et al. (2022) adopted a similar approach to analyze how factors such as production time influence fracture complexity during refracturing. Recently, Shi et al. (2024) developed a hydro-mechanically coupled XFEM model to investigate production-induced stress changes, HF propagation, and the optimization of refracturing treatments.

Despite these advances, most existing studies primarily focus on depletion-induced stress changes and their impacts on infill or refracturing operations. The influence of pre-fracturing EE on subsequent fracture initiation and propagation has not been systematically investigated. Moreover, due to the disparate temporal and spatial scales involved in these two stages (Zhang et al., 2022), EE and hydraulic fracturing are often treated as independent processes, neglecting their sequential and strongly coupled nature. To address this gap, this study conducts an integrated and sequential simulation of the EE and hydraulic fracturing process, in which the coupled evolution of pore pressure, stress redistribution, and fracture propagation is consistently captured within a unified hydro-mechanical XFEM framework. Based on this integrated modeling approach, the study systematically investigates how operational (e.g., injection volume, rate, fluid viscosity, shut-in time, initiation location) and geological (e.g., matrix permeability) parameters influence injection pressure, fracturing efficiency, and fracture geometry. The results provide quantitative guidelines for optimizing energy-enhanced fracturing designs in low-permeability reservoirs.

2. Problem formulation

Fig. 1 presents the two-stage development strategy for low-pressure, low-permeability reservoirs in China. In the first stage (EE), fluids are injected to raise the formation pressure while displacing in-situ crude oil from the reservoir. Once the formation pressure reaches the target value, subsequent hydraulic fracturing is performed to improve well productivity by creating conductive fracture networks. The EE stage involves two key mechanisms, namely fluid migration through the porous matrix and matrix

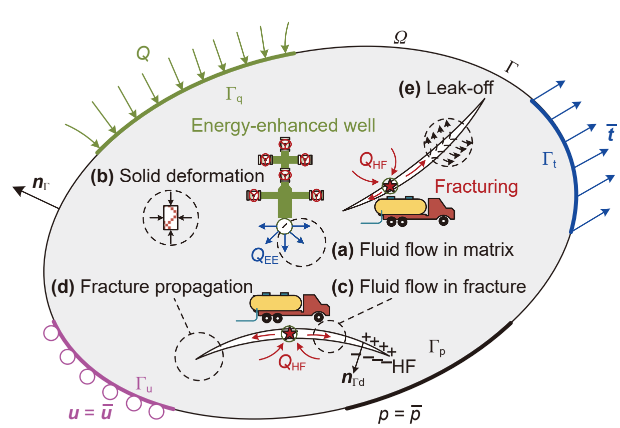

Fig. 1. Schematic of energy enhancement and subsequent hydraulic fracturing. (**a**) Matrix deformation, (**b**) matrix fluid flow, (**c**) fracture fluid flow, (**d**) fracture propagation, and (**e**) fluid leak-off.

deformation driven by pressure gradients. The injection pressure is kept below the breakdown pressure to avoid initiating fractures. Subsequent hydraulic fracturing uses a higher injection rate to stimulate the reservoir and induces more complex behavior. Although energy-enhanced and fracturing fluids differ in properties such as viscosity, their flow within the matrix follows Darcy's law. Thus, the integrated process (EE and hydraulic fracturing) comprises five fundamental mechanisms, as shown in Fig. 1.

This study investigates how stress and pressure redistribution induced by EE influence fracture growth patterns during subsequent hydraulic fracturing. To simplify the modeling, the matrix is treated as a homogeneous, saturated porous medium, and the energy-enhanced fluid is assumed to share identical properties with the native reservoir fluid. The two-dimensional model shown in Fig. 1 includes an energy-enhanced injection well that introduces the enhancement fluid at a constant rate Q_{EE}, resulting in pressure and stress variations within the formation. The model boundary Γ has an outward normal vector $\boldsymbol{n}_\Gamma$. Displacement and traction boundary conditions are applied on Γ_u and Γ_t, respectively, satisfying $\Gamma_u \cup \Gamma_t = \Gamma$ and $\Gamma_u \cap \Gamma_t = \emptyset$. Similarly, pore pressure and flow boundaries are defined on Γ_p and Γ_q, with $\Gamma_p \cup \Gamma_q = \Gamma$ and $\Gamma_p \cap \Gamma_q = \emptyset$. Hydraulic fracturing is initiated at or near the injection well by injecting fracturing fluid at a rate Q_{HF}, which drives fracture propagation. The fracture is represented by two opposing faces: the positive face Γ_d^+ and the negative face Γ_d^-, with outward normal vectors $\boldsymbol{n}_{\Gamma d}^+$ and $\boldsymbol{n}_{\Gamma d}^-$, respectively. These vectors satisfy $\boldsymbol{n}_{\Gamma d} = \boldsymbol{n}_{\Gamma d}^+ = -\boldsymbol{n}_{\Gamma d}^-$, and the union $\Gamma_d^+ \cup \Gamma_d^-$ defines the fracture flow domain.

The mechanical boundary conditions are given by:

$$\boldsymbol{u} = \bar{\boldsymbol{u}} \text{ on } \Gamma_u \text{ and } \boldsymbol{\sigma} \cdot \boldsymbol{n}_\Gamma = \bar{\boldsymbol{t}} \text{ on } \Gamma_t \tag{1}$$

where $\bar{\boldsymbol{u}}$ is the prescribed displacement and $\bar{\boldsymbol{t}}$ is the prescribed traction, and $\boldsymbol{\sigma}$ is the Cauchy stress tensor.

The fluid boundary conditions are defined as:

$$p = \bar{p} \text{ on } \Gamma_p \text{ and } Q = \boldsymbol{v}_w \cdot \boldsymbol{n}_\Gamma \text{ on } \Gamma_q \tag{2}$$

where $\bar{p}$ is the prescribed pore pressure, $\boldsymbol{v}_w$ is the Darcy velocity, and Q denotes the prescribed flow rate across the computational boundary, which corresponds to the injection rate during EE (Q_{EE}) or hydraulic fracturing (Q_{HF}), depending on the simulation stage.

The pressure applied by the fracturing fluid on the fracture surface is expressed as:

$$\boldsymbol{\sigma} \cdot \boldsymbol{n}_{\Gamma d} = -p_f \boldsymbol{n}_{\Gamma d} \text{ on } \Gamma_d \tag{3}$$

where p_f is the fluid pressure imposed on the fracture face. In addition, the fluid exchange between the fracture and matrix, i.e., leak-off, is described by:

$$q_f = [\![\boldsymbol{v}_w]\!] \cdot \boldsymbol{n}_{\Gamma d} \text{ on } \Gamma_d \tag{4}$$

where $[\![\boldsymbol{v}_w]\!] = \boldsymbol{v}_w^+ - \boldsymbol{v}_w^-$ represents the difference in the normal fluid velocity between the positive and the negative fracture surface. Hence, q_f represents the leakage rate of the fracturing fluid per unit area of the fracture surface. The governing equations for different physical processes are presented in the following section.

2.1. Governing equations

2.1.1. Solid deformation

To compute the mechanical response of a single-phase, homogeneous saturated porous medium, the linear elastic momentum conservation equation can be expressed based on Biot's effective stress principle as:

$$\nabla \cdot (\boldsymbol{\sigma}' - \alpha p \boldsymbol{I}) + \rho(\boldsymbol{b} - \ddot{\boldsymbol{u}}) = \boldsymbol{0} \tag{5}$$

where $\boldsymbol{\sigma}'$ denotes the effective stress tensor ($\boldsymbol{\sigma} = \boldsymbol{\sigma}' - \alpha p \boldsymbol{I}$), α is the Biot coefficient, and $\rho = \phi\rho_f + (1-\phi)\rho_s$ represents the average density of the reservoir, accounting for both solid matrix and pore fluid. Here, ϕ is the porosity, ρ_f is the fluid density, ρ_s is the solid density, $\boldsymbol{b}$ denotes the body force vector, and $\ddot{\boldsymbol{u}}$ is the solid phase acceleration. According to Hooke's law, the relationship between effective stress and total strain can be written as:

$$\boldsymbol{\sigma}' = \boldsymbol{D} : \boldsymbol{\varepsilon} \tag{6}$$

where $\boldsymbol{D}$ is the elastic constitutive matrix and $\boldsymbol{\varepsilon}$ is the strain tensor.

2.1.2. Fluid flow in matrix

The momentum conservation equation for the fluid phase can be formulated by neglecting its relative acceleration with respect to the solid phase (Zienkiewicz et al., 1999; Khoei, 2014):

$$-\nabla p - \boldsymbol{R} + \rho_f(\boldsymbol{b} - \ddot{\boldsymbol{u}}) = \boldsymbol{0} \tag{7}$$

where $\boldsymbol{R}$ denotes the viscous drag force exerted by the solid phase on the fluid phase, with dimensions $[M][L]^{-2}[T]^{-2}$. Based on Darcy's law, the relationship between seepage force and fluid velocity can be expressed as:

$$\boldsymbol{v}_m = \frac{\boldsymbol{k}_m}{\mu_f} \boldsymbol{R} \tag{8}$$

where $\boldsymbol{v}_m$ represents the matrix fluid velocity ($[L][T]^{-1}$), $\boldsymbol{k}_m$ is the matrix permeability ($[L]^2$), and μ_f denotes the fluid viscosity, which corresponds to either that of the energy-enhanced fluid (μ_{EE}) or the fracturing fluid (μ_{HF}). In addition, the mass conservation equation for the fluid phase can be written as:

$$\nabla \cdot \boldsymbol{v}_m + \alpha \nabla \cdot \dot{\boldsymbol{u}} + \dot{p}/K_r = \boldsymbol{0} \tag{9}$$

where $\dot{\boldsymbol{u}}$ is the solid phase velocity,and $\dot{p}$ is the time derivative of the fluid pressure. The parameter $K_r = K_s K_f / (K_f(\alpha - \phi) + K_s \phi)$ denotes the reservoir compressibility modulus, where K_s and K_f are the bulk moduli of the reservoir solid phase and the pore fluid, respectively. By combining Eqs. (7)–(9), the following governing equation is obtained:

$$\nabla \cdot \left\{ \frac{\boldsymbol{k}_m}{\mu_f} \left[-\nabla p + \rho_f(\boldsymbol{b} - \ddot{\boldsymbol{u}}) \right] \right\} + \alpha \nabla \cdot \dot{\boldsymbol{u}} + \dot{p} \Big/ K_r = \boldsymbol{0} \tag{10}$$

2.1.3. Fluid flow in fracture

The fluid mass balance within a fracture follows a continuity equation analogous to the matrix domain (Eq. (9)):

$$\nabla \cdot \boldsymbol{v}_f + \nabla \cdot \dot{\boldsymbol{u}} + \dot{p} \Big/ K_f = \boldsymbol{0} \tag{11}$$

where $\boldsymbol{v}_f$ denotes the fluid velocity along the fracture. Based on Darcy's law, this velocity can be related to the pressure gradient through:

$$\boldsymbol{v}_f = \frac{k_f}{\mu_f} \left[-\nabla p + \rho_f(\boldsymbol{b} - \ddot{\boldsymbol{u}}) \right] \tag{12}$$

where k_f denotes fracture permeability, which is governed by the cubic law (Witherspoon et al., 1980). This empirical relationship expresses permeability as a function of fracture aperture w_N:

$$k_{\mathrm{f}} = \frac{w_{\mathrm{N}}^2}{12} \tag{13}$$

By substituting Eqs. (12) and (13) into Eq. (11), the governing equation describing fluid flow within the fracture is derived as:

$$\nabla \cdot \left\{ \frac{k_{\mathrm{f}}}{\mu_{\mathrm{f}}} \left[-\nabla p + \rho_{\mathrm{f}}(\boldsymbol{b} - \ddot{\boldsymbol{u}}) \right] \right\} + \nabla \cdot \dot{\boldsymbol{u}} + \dot{p} \Big/ K_{\mathrm{f}} = \boldsymbol{0} \tag{14}$$

2.1.4. Fracture propagation

This study adopts linear elastic fracture mechanics to evaluate the mechanical behavior at fracture tips. To accurately model fracture propagation, the interaction integral method (Moës and Belytschko, 2002) is applied to compute the Mode I and Mode II stress intensity factors (K_{I} and K_{II}) at the fracture tip. Fracture growth is predicted using the maximum circumferential stress criterion (Erdogan and Sih, 1963), which states that propagation occurs when the equivalent stress intensity factor exceeds the fracture toughness of the material ($K_{\mathrm{eq}} > K_{\mathrm{Ic}}$). The equivalent stress intensity factor is given by:

$$K_{\mathrm{eq}} = \cos\frac{\theta_{\mathrm{p}}}{2}\left(K_{\mathrm{I}}\cos^2\frac{\theta_{\mathrm{p}}}{2} - \frac{3K_{\mathrm{II}}}{2}\sin\theta_{\mathrm{p}}\right) \tag{15}$$

where θ_{p} represents the propagation direction, which can be determined by (Paris and Sih, 1965):

$$\theta_{\mathrm{p}} = 2\arctan\frac{1}{4}\left[\frac{K_{\mathrm{I}}}{K_{\mathrm{II}}} - \mathrm{sign}(K_{\mathrm{II}})\sqrt{\left(\frac{K_{\mathrm{I}}}{K_{\mathrm{II}}}\right)^2 + 8}\right] \tag{16}$$

2.2. Weak forms

The weak form of the momentum conservation equation for the matrix is obtained by multiplying Eq. (5) by the displacement test function $\delta\boldsymbol{u}$ and integrating over the two-dimensional domain Ω. Applying the divergence theorem to Γ_{t} and Γ_{d}, and imposing the boundary conditions from Eqs. (1) and (3), yields:

$$\begin{aligned}&\int_{\Gamma_{\mathrm{t}}} \delta\boldsymbol{u}\cdot\bar{\boldsymbol{t}}\mathrm{d}\Gamma - \int_{\Gamma_{\mathrm{d}}} [\![\delta\boldsymbol{u}]\!]\cdot p_{\mathrm{f}}\boldsymbol{n}_{\Gamma\mathrm{d}}\mathrm{d}\Gamma - \int_{\Omega}\nabla\delta\boldsymbol{u} : \boldsymbol{\sigma}\mathrm{d}\Omega + \int_{\Omega}\delta\boldsymbol{u}\rho(\boldsymbol{b} - \ddot{\boldsymbol{u}})\mathrm{d}\Omega \\ &= 0\end{aligned} \tag{17}$$

where $[\![\delta\boldsymbol{u}]\!] = \delta\boldsymbol{u}^+ - \delta\boldsymbol{u}^-$ represents the displacement jump across the fracture interface.

Following a similar approach, the weak form of the matrix fluid flow continuity equation is derived by multiplying Eq. (10) by the pore pressure test function δp and integrating over Ω. Applying the divergence theorem to Γ_{q} and Γ_{d}, and imposing the boundary conditions given in Eq. (2), results in:

$$\begin{aligned}&\int_{\Gamma_{\mathrm{q}}} \delta p\cdot Q\mathrm{d}\Gamma + \int_{\Gamma_{\mathrm{d}}} \delta p\cdot [\![\boldsymbol{v}_{\mathrm{w}}]\!]\, n_{\Gamma\mathrm{d}}\mathrm{d}\Gamma - \int_{\Omega}\nabla\delta p\cdot\boldsymbol{v}_{\mathrm{w}}\mathrm{d}\Omega + \int_{\Omega}\delta p\alpha\nabla\cdot\dot{\boldsymbol{u}}\mathrm{d}\Omega \\ &+ \int_{\Omega}\delta p\frac{\dot{p}}{K_{\mathrm{r}}}\mathrm{d}\Omega \\ &= 0\end{aligned} \tag{18}$$

where $[\![\boldsymbol{v}_{\mathrm{w}}]\!] = \boldsymbol{v}_{\mathrm{w}}^+ - \boldsymbol{v}_{\mathrm{w}}^-$ represents the difference in fluid velocity across the fracture surface.

For the fracture domain, the weak form of the flow continuity equation is derived by multiplying Eq. (14) by the pore pressure test function δp and integrating over the fracture domain Ω':

$$\int_{\Gamma_{\mathrm{d}}} \delta p q_{\mathrm{f}}\mathrm{d}\Gamma - \int_{\Omega'}\delta p\nabla\cdot\dot{\boldsymbol{u}}\mathrm{d}\Omega' - \int_{\Omega'}\delta p\frac{\dot{p}}{K_{\mathrm{f}}}\mathrm{d}\Omega' + \int_{\Omega'}\nabla\delta p\cdot\boldsymbol{v}_{\mathrm{f}}\mathrm{d}\Omega' = 0 \tag{19}$$

Incorporating the leak-off boundary condition from Eq. (4) and integrating along the fracture surface Γ_{d}, the following expression is obtained:

$$\begin{aligned}&\int_{\Gamma_{\mathrm{d}}} \delta p\cdot [\![\boldsymbol{v}_{\mathrm{w}}]\!]\, n_{\Gamma\mathrm{d}}\mathrm{d}\Gamma = \int_{\Omega'}\delta p\nabla\cdot\dot{\boldsymbol{u}}\mathrm{d}\Omega' + \int_{\Omega'}\delta p\frac{\dot{p}}{K_{\mathrm{f}}}\mathrm{d}\Omega' \\ &- \int_{\Omega'}\nabla\delta p\cdot\boldsymbol{v}_{\mathrm{f}}\mathrm{d}\Omega' = 0\end{aligned} \tag{20}$$

In summary, Eq. (17) provides the weak form of the momentum balance equation for solid deformation, while the combined weak forms of Eqs. (18) and (20) describe fluid flow in the matrix and fracture domains.

3. Numerical method

3.1. XFEM approximation

3.1.1. Approximation of u(x,t)

Based on the concept of partition of unity (Melenk and Babuška, 1996), the XFEM approximation of the displacement field is achieved by incorporating appropriate enrichment functions into the standard finite element approximation. In this study, a Heaviside function is incorporated to describe the displacement discontinuities across the fracture, along with asymptotic crack-tip functions to represent the stress singularity. The enrichment strategies for a single fracture follow the approaches detailed in Moës et al. (1999) and Belytschko and Black (1999). Accordingly, the XFEM approximation of the displacement can be expressed as:

$$\boldsymbol{u}(\boldsymbol{x},t) = \underbrace{\boldsymbol{N}_{\mathrm{u}}^{\mathrm{Std}}(\boldsymbol{x})\bar{\boldsymbol{u}}(t)}_{\text{Continuous part}} + \underbrace{\boldsymbol{N}_{\mathrm{u}}^{\mathrm{Hev}}(\boldsymbol{x})\bar{\boldsymbol{a}}(t)}_{\text{Discontinuous part}} + \underbrace{\boldsymbol{N}_{\mathrm{u}}^{\mathrm{Tip}}(\boldsymbol{x})\bar{\boldsymbol{b}}(t)}_{\text{Singular part}} \tag{21}$$

where $\boldsymbol{N}_i(\boldsymbol{x})$ (for i = 1 to 4) are the bilinear shape functions associated with four-node quadrilateral elements, and $\boldsymbol{N}_{\mathrm{u}}^{\mathrm{Std}}(\boldsymbol{x}) = [\boldsymbol{N}_i(\boldsymbol{x})]$ is the matrix of standard displacement shape functions. For nodes enriched to capture the displacement step, the corresponding shape functions are denoted $\boldsymbol{N}_{ia}(\boldsymbol{x})$, and $\boldsymbol{N}_{\mathrm{u}}^{\mathrm{Hev}}(\boldsymbol{x}) = [\boldsymbol{N}_{ia}(\boldsymbol{x})(H(\boldsymbol{x}) - H(\boldsymbol{x}_{ia}))]$ is the matrix of enriched shape functions associated with the Heaviside function $H(\boldsymbol{x})$. For nodes near the fracture tip, the enrichment is defined by shape functions $\boldsymbol{N}_{ib}(\boldsymbol{x})$, and $\boldsymbol{N}_{\mathrm{u}}^{\mathrm{Tip}}(\boldsymbol{x}) = [\boldsymbol{N}_{ib}(\boldsymbol{x})(B(\boldsymbol{x}) - B(\boldsymbol{x}_{ib}))]$ is the matrix of enriched shape functions associated with the asymptotic crack-tip functions $B(\boldsymbol{x})$. The detailed expressions for $\boldsymbol{N}_i(\boldsymbol{x})$, $\boldsymbol{N}_{ia}(\boldsymbol{x})$, $\boldsymbol{N}_{ib}(\boldsymbol{x})$ are provided in our previous work (Zhou et al., 2020). The symbols $\bar{\boldsymbol{u}}$, $\bar{\boldsymbol{a}}$, $\bar{\boldsymbol{b}}$ represent the standard and enriched degrees of freedom of the displacement field, and $\bar{\boldsymbol{U}} = [\bar{\boldsymbol{u}} \;\; \bar{\boldsymbol{a}} \;\; \bar{\boldsymbol{b}}]$ defines the vector of assembled nodal displacement variables.

3.1.2. Approximation of p(x,t)

Similar to the displacement field approximation, the XFEM represents the pressure field by combining the standard approximation with enrichment functions. The influence of a fracture on the pressure field is characterized as a weak discontinuity, where pressure remains continuous across the fractures, but its normal gradient is discontinuous (Khoei, 2014; Réthoré et al., 2007). To capture this characteristic, the ridge function is employed to enrich elements intersected by fractures (Moës et al., 2003). Consequently, the XFEM approximation of the pressure field can be expressed as:

$$p(\boldsymbol{x},t)=\underbrace{\boldsymbol{N}_{\mathrm{p}}^{\mathrm{Std}}(\boldsymbol{x})\overline{\boldsymbol{p}}(t)}_{\text{Continuous part}}+\underbrace{\boldsymbol{N}_{\mathrm{p}}^{\mathrm{Rid}}(\boldsymbol{x})\overline{\boldsymbol{c}}(t)}_{\text{Gradient discontinuity part}}\tag{22}$$

where $\boldsymbol{N}_{\mathrm{p}}^{\mathrm{Std}}(\boldsymbol{x})=[N_i(\boldsymbol{x})]$ (for $i=1$ to 4) denotes the standard pressure shape function matrix constructed from the same bilinear shape functions as the displacement field. For nodes enriched to capture fracture-induced weak discontinuities, $\boldsymbol{N}_{\mathrm{p}}^{\mathrm{Rid}}(\boldsymbol{x})$ represents the corresponding enriched shape functions, and $\boldsymbol{N}_{\mathrm{p}}^{\mathrm{Rid}}(\boldsymbol{x})=[\boldsymbol{N}_{\mathrm{ic}}(\boldsymbol{x})(\psi(\boldsymbol{x})-\psi(\boldsymbol{x}_{\mathrm{ic}}))]$ is the matrix of enriched shape functions associated with the ridge function $\psi(\boldsymbol{x})$. Detailed expressions for $\boldsymbol{N}_{\mathrm{ic}}(\boldsymbol{x})$ and $\psi(\boldsymbol{x})$ are provided in the seminal work by Moës et al. (2003). The symbols $\overline{\boldsymbol{p}}$, $\overline{\boldsymbol{c}}$ correspond to the standard and enriched DOF of the pressure field, respectively, while $\overline{\boldsymbol{P}}=[\overline{\boldsymbol{p}}\quad\overline{\boldsymbol{c}}]$ represents the vector of assembled nodal pressure variables.

3.2. Spatial and time discretization

By defining the variations of displacement and pressure ($\delta\boldsymbol{u}$ and δp) within the same enriched approximation spaces as $\boldsymbol{u}$ and p, respectively, and subsequently substituting the test functions $\delta\boldsymbol{u}(\boldsymbol{x}, t)$ and $\delta p(p, t)$ into the weak forms of the equilibrium and the continuity equations, the discretized u-p coupled equations are obtained:

$$\begin{cases}\boldsymbol{M}\ddot{\overline{\boldsymbol{U}}}+\boldsymbol{K}\overline{\boldsymbol{U}}-\boldsymbol{Q}\overline{\boldsymbol{P}}+\boldsymbol{f}^{\mathrm{int}}-\boldsymbol{f}^{\mathrm{ext}}=\boldsymbol{0}\\ \boldsymbol{C}\ddot{\overline{\boldsymbol{U}}}+\boldsymbol{H}\overline{\boldsymbol{P}}+\boldsymbol{Q}^{\mathrm{T}}\dot{\overline{\boldsymbol{U}}}+\boldsymbol{S}\dot{\overline{\boldsymbol{P}}}+\boldsymbol{q}^{\mathrm{int}}-\boldsymbol{q}^{\mathrm{ext}}=\boldsymbol{0}\end{cases}\tag{23}$$

where $\boldsymbol{M}$ is the solid mass matrix, $\boldsymbol{K}$ is the stiffness matrix, $\boldsymbol{Q}$ is the coupling matrix, $\boldsymbol{f}^{\mathrm{int}}$ is the internal force vector, $\boldsymbol{f}^{\mathrm{ext}}$ is the external force vector, $\boldsymbol{C}$ is the fluid mass matrix, $\boldsymbol{H}$ is the permeability matrix, $\boldsymbol{S}$ is the compressibility matrix, $\boldsymbol{q}^{\mathrm{int}}$ is the internal flux vector, and $\boldsymbol{q}^{\mathrm{ext}}$ is the external flux vector. The specific expressions for these terms are provided in Table 1.

It is noted that in Table 1, $\boldsymbol{N}_{\mathrm{p}}^{\gamma}$ and $\boldsymbol{N}_{\mathrm{p}}^{\delta}$ ((γ, δ)∈(Std, Rid)) are standard or enriched pressure shape function matrices, while $\boldsymbol{B}_{\mathrm{u}}^{\alpha}$ and $\boldsymbol{B}_{\mathrm{u}}^{\beta}$ ((α, β)∈(Std, Hev, Tip)) are standard or enriched discretized gradient operators, satisfying $\boldsymbol{\varepsilon}=\boldsymbol{B}_{\mathrm{u}}^{\alpha}\boldsymbol{U}$. The symbol $[\![\boldsymbol{N}_{\mathrm{u}}^{\alpha}]\!]=(\boldsymbol{N}_{\mathrm{u}}^{\alpha})^{+}-(\boldsymbol{N}_{\mathrm{u}}^{\alpha})^{-}$ denotes the jump of the displacement shape function across the fracture surface, $\langle N_{\mathrm{u}}^{\alpha}\rangle=\left((N_{\mathrm{u}}^{\alpha})^{+}+(N_{\mathrm{u}}^{\alpha})^{-}\right)/2$ represents its average value across the fracture surface, and $\boldsymbol{m}_{\Gamma\mathrm{d}}$ is the unit tangential vector of the fracture, obtained by rotating the normal vector $\boldsymbol{n}_{\Gamma\mathrm{d}}$ clockwise by 90°.

For temporal discretization, the generalized Newmark scheme is employed to compute the velocity, acceleration, and the rate of pressure change. Consequently, the unknown variables at time t_{n+1} can be determined from the known variables at time t_n:

$$\begin{aligned}\ddot{\overline{\boldsymbol{U}}}_{n+1}&=\frac{1}{a_1\Delta t^2}(\overline{\boldsymbol{U}}_{n+1}-\overline{\boldsymbol{U}}_n)-\frac{1}{a_1\Delta t}\dot{\overline{\boldsymbol{U}}}_n-\left(\frac{1}{2a_1}-1\right)\ddot{\overline{\boldsymbol{U}}}_n\\ \dot{\overline{\boldsymbol{U}}}_{n+1}&=\frac{a_2}{a_1\Delta t}(\overline{\boldsymbol{U}}_{n+1}-\overline{\boldsymbol{U}}_n)-\left(\frac{a_2}{a_1}-1\right)\dot{\overline{\boldsymbol{U}}}_n-\Delta t\left(\frac{a_2}{2a_1}-1\right)\ddot{\overline{\boldsymbol{U}}}_n\\ \dot{\overline{\boldsymbol{P}}}_{n+1}&=\frac{1}{b_1\Delta t}(\overline{\boldsymbol{P}}_{n+1}-\overline{\boldsymbol{P}}_n)-\left(\frac{1}{b_1}-1\right)\dot{\overline{\boldsymbol{P}}}_n\end{aligned}\tag{24}$$

where $\Delta t=t_{n+1}-t_n$ is the current time step size. To ensure unconditional stability of the time integration, the parameters a_1, a_2, and b_1 must satisfy the conditions: $a_1\geq 0.25(0.5+a_2)^2$, $a_2\geq 0.5$, and $b_1\geq 0.5$. Substituting Eq. (24) into Eq. (23) yields the residual of the u-p coupled discretized equations at t_{n+1}:

$$\begin{cases}\boldsymbol{R}_{n+1}^{\mathrm{u}}=\dfrac{\boldsymbol{M}}{a_1\Delta t^2}\overline{\boldsymbol{U}}_{n+1}+\boldsymbol{K}\overline{\boldsymbol{U}}_{n+1}-\boldsymbol{Q}\overline{\boldsymbol{P}}_{n+1}+\boldsymbol{f}_{n+1}^{\mathrm{int}}-\boldsymbol{G}_{n+1}^{\mathrm{u}}\\ \boldsymbol{R}_{n+1}^{\mathrm{p}}=\dfrac{\boldsymbol{C}}{a_1\Delta t^2}\overline{\boldsymbol{U}}_{n+1}+\boldsymbol{H}\overline{\boldsymbol{P}}_{n+1}+\dfrac{a_2\boldsymbol{Q}^T}{a_1\Delta t}\overline{\boldsymbol{U}}_{n+1}+\dfrac{\boldsymbol{S}}{b_1\Delta t}\overline{\boldsymbol{P}}_{n+1}\\ +\boldsymbol{q}_{n+1}^{\mathrm{int}}-\boldsymbol{G}_{n+1}^{\mathrm{p}}\end{cases}\tag{25}$$

where $\boldsymbol{G}_{n+1}^{\mathrm{u}}$ and $\boldsymbol{G}_{n+1}^{\mathrm{p}}$ are known quantities at time t_n, defined as:

$$\begin{cases}\boldsymbol{G}_{n+1}^{\mathrm{u}}=\boldsymbol{M}\left(\dfrac{1}{a_1\Delta t^2}\overline{\boldsymbol{U}}_n+\dfrac{1}{a_1\Delta t}\dot{\overline{\boldsymbol{U}}}_n+\left(\dfrac{1}{2a_1}-1\right)\ddot{\overline{\boldsymbol{U}}}_n\right)+\boldsymbol{f}_{n+1}^{\mathrm{ext}}\\ \boldsymbol{G}_{n+1}^{\mathrm{p}}=\boldsymbol{C}\left(\dfrac{1}{a_1\Delta t^2}\overline{\boldsymbol{U}}_n+\dfrac{1}{a_1\Delta t}\dot{\overline{\boldsymbol{U}}}_n+\left(\dfrac{1}{2a_1}-1\right)\ddot{\overline{\boldsymbol{U}}}_n\right)\\ +\boldsymbol{Q}^{\mathrm{T}}\left(\dfrac{a_2}{a_1\Delta t}\overline{\boldsymbol{U}}_n+\left(\dfrac{a_2}{a_1}-1\right)\dot{\overline{\boldsymbol{U}}}_n+\Delta t\left(\dfrac{1}{2a_1}-1\right)\ddot{\overline{\boldsymbol{U}}}_n\right)\\ +\boldsymbol{S}\left(\dfrac{1}{b_1\Delta t}\overline{\boldsymbol{P}}_n+\left(\dfrac{1}{b_1}-1\right)\dot{\overline{\boldsymbol{P}}}_n\right)+\boldsymbol{q}_{n+1}^{\mathrm{ext}}\end{cases}\tag{26}$$

3.3. Solution strategy

In this study, the Newton–Raphson iteration method is employed to efficiently solve the discretized u-p equations. The Jacobian matrix $\boldsymbol{J}$ comprises partial derivatives of the residual with

Table 1
The expression of each term in Eq. (23).

Force related terms	Flux related terms
$\boldsymbol{M}=\int_\Omega(\boldsymbol{N}_{\mathrm{u}}^{\alpha})^{\mathrm{T}}\rho\boldsymbol{N}_{\mathrm{u}}^{\beta}\mathrm{d}\Omega$	$\boldsymbol{C}=\int_\Omega\left(\nabla\boldsymbol{N}_{\mathrm{p}}^{\gamma}\right)^{\mathrm{T}}\boldsymbol{k}_{\mathrm{m}}\rho_{\mathrm{f}}\boldsymbol{N}_{\mathrm{u}}^{\alpha}\mathrm{d}\Omega$
$\boldsymbol{K}=\int_\Omega(\boldsymbol{B}_{\mathrm{u}}^{\alpha})^{\mathrm{T}}\boldsymbol{D}\boldsymbol{B}_{\mathrm{u}}^{\beta}\mathrm{d}\Omega$	$\boldsymbol{H}=\int_\Omega\left(\nabla\boldsymbol{N}_{\mathrm{p}}^{\gamma}\right)^{\mathrm{T}}\boldsymbol{k}_{\mathrm{m}}\left(\nabla\boldsymbol{N}_{\mathrm{p}}^{\delta}\right)\mathrm{d}\Omega$
$\boldsymbol{Q}=\int_\Omega(\boldsymbol{B}_{\mathrm{u}}^{\alpha})^{\mathrm{T}}\alpha\boldsymbol{I}\boldsymbol{N}_{\mathrm{p}}^{\beta}\mathrm{d}\Omega$	$\boldsymbol{S}=\int_\Omega\left(\boldsymbol{N}_{\mathrm{p}}^{\gamma}\right)^{\mathrm{T}}\boldsymbol{N}_{\mathrm{p}}^{\delta}/K_{\mathrm{r}}\mathrm{d}\Omega$
$\boldsymbol{f}^{\mathrm{int}}=\int_{\Gamma_{\mathrm{d}}}[\![\boldsymbol{N}_{\mathrm{u}}^{\alpha}]\!]^{\mathrm{T}}p_{\mathrm{f}}\boldsymbol{n}_{\Gamma_{\mathrm{d}}}\mathrm{d}\Gamma$	$\boldsymbol{q}^{\mathrm{int}}=\int_{\Gamma_{\mathrm{d}}}\left(\boldsymbol{N}_{\mathrm{p}}^{\gamma}\right)^{\mathrm{T}}[\![\boldsymbol{v}_{\mathrm{w}}]\!]\cdot\boldsymbol{n}_{\Gamma\mathrm{d}}\mathrm{d}\Gamma$
$\boldsymbol{f}^{\mathrm{ext}}=\int_\Omega(\boldsymbol{N}_{\mathrm{u}}^{\alpha})^{\mathrm{T}}\rho\boldsymbol{b}\mathrm{d}\Omega+\int_{\Gamma_{\mathrm{t}}}(\boldsymbol{N}_{\mathrm{u}}^{\alpha})^{\mathrm{T}}\overline{\boldsymbol{t}}\mathrm{d}\Gamma$	$\boldsymbol{q}^{\mathrm{ext}}=\int_\Omega\left(\nabla\boldsymbol{N}_{\mathrm{p}}^{\gamma}\right)^{\mathrm{T}}\boldsymbol{k}_{\mathrm{w}}\rho_{\mathrm{f}}\boldsymbol{b}\mathrm{d}\Omega-\int_{\Gamma_{\mathrm{q}}}\left(\boldsymbol{N}_{\mathrm{p}}^{\gamma}\right)^{\mathrm{T}}Q\mathrm{d}\Gamma$
$\boldsymbol{q}^{\mathrm{int}}=\int_{\Gamma_{\mathrm{d}}}k_{\mathrm{f}}w_{\mathrm{N}}\left(\nabla\boldsymbol{N}_{\mathrm{p}}^{\gamma}\right)^{\mathrm{T}}(\boldsymbol{m}_{\Gamma\mathrm{d}})^{\mathrm{T}}\boldsymbol{m}_{\Gamma\mathrm{d}}\nabla\boldsymbol{N}_{\mathrm{p}}^{\delta}\mathrm{d}\Gamma\overline{\boldsymbol{P}}-\int_{\Gamma_{\mathrm{d}}}\left(\boldsymbol{N}_{\mathrm{p}}^{\gamma}\right)^{\mathrm{T}}(\boldsymbol{n}_{\Gamma\mathrm{d}})^{\mathrm{T}}[\![\boldsymbol{N}_{\mathrm{u}}^{\alpha}]\!]\mathrm{d}\Gamma\dot{\overline{\boldsymbol{U}}}+\int_{\Gamma_{\mathrm{d}}}w_{\mathrm{N}}\left(\boldsymbol{N}_{\mathrm{p}}^{\gamma}\right)^{\mathrm{T}}(\boldsymbol{m}_{\Gamma\mathrm{d}})^{\mathrm{T}}\boldsymbol{m}_{\Gamma\mathrm{d}}\langle\nabla\boldsymbol{N}_{\mathrm{u}}^{\alpha}\rangle\mathrm{d}\Gamma\dot{\overline{\boldsymbol{U}}}+\int_{\Gamma_{\mathrm{d}}}w_{\mathrm{N}}\left(\boldsymbol{N}_{\mathrm{p}}^{\gamma}\right)^{\mathrm{T}}\boldsymbol{N}_{\mathrm{p}}^{\delta}/K_{\mathrm{f}}\mathrm{d}\Gamma\dot{\overline{\boldsymbol{P}}}-\int_{\Gamma_{\mathrm{d}}}k_{\mathrm{f}}w_{\mathrm{N}}\rho_{\mathrm{f}}\left(\nabla\boldsymbol{N}_{\mathrm{p}}^{\gamma}\right)^{T}(\boldsymbol{m}_{\Gamma\mathrm{d}})^{T}\boldsymbol{m}_{\Gamma\mathrm{d}}\boldsymbol{b}\mathrm{d}\Gamma+\int_{\Gamma_{\mathrm{d}}}k_{\mathrm{f}}w_{\mathrm{N}}\rho_{\mathrm{f}}\left(\nabla\boldsymbol{N}_{\mathrm{p}}^{\gamma}\right)^{T}(\boldsymbol{m}_{\Gamma\mathrm{d}})^{T}\boldsymbol{m}_{\Gamma\mathrm{d}}\langle\boldsymbol{N}_{\mathrm{u}}^{\alpha}\rangle\mathrm{d}\Gamma\ddot{\overline{\boldsymbol{U}}}$	

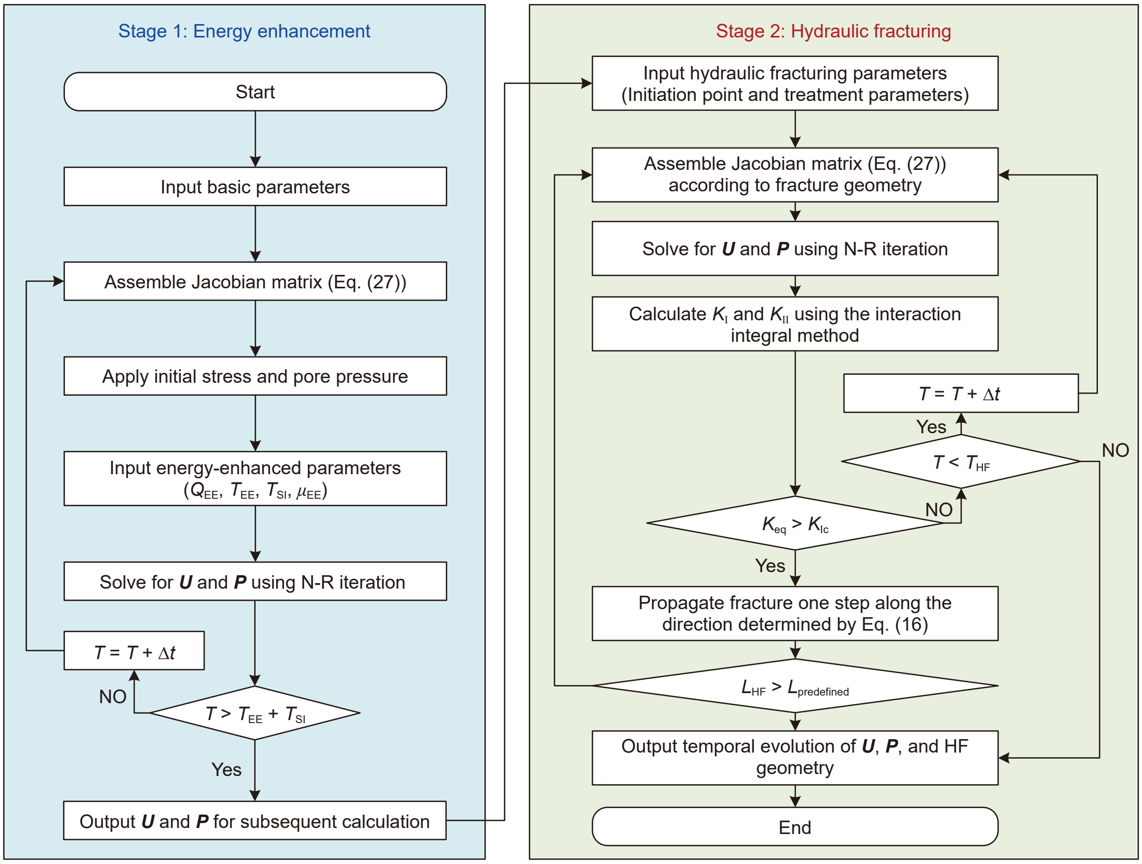

Fig. 2. Solving strategy of energy enhancement and subsequent hydraulic fracturing.

respect to the global displacement vector $\boldsymbol{U}$ and the global pressure vector $\boldsymbol{P}$:

$$\boldsymbol{J}=\begin{bmatrix} \dfrac{\boldsymbol{M}}{a_1\Delta t^2}+\boldsymbol{K}+\dfrac{\partial \boldsymbol{f}^{\text{int}}}{\partial \boldsymbol{U}} & \dfrac{\partial \boldsymbol{f}^{\text{int}}}{\partial \boldsymbol{P}}-\boldsymbol{Q} \\ \dfrac{\boldsymbol{C}}{a_1\Delta t^2}+\dfrac{a_2\boldsymbol{Q}^T}{a_1\Delta t}+\dfrac{\partial \boldsymbol{q}^{\text{int}}}{\partial \boldsymbol{U}} & \boldsymbol{H}+\dfrac{\boldsymbol{S}}{b_1\Delta t}+\dfrac{\partial \boldsymbol{q}^{\text{int}}}{\partial \boldsymbol{P}} \end{bmatrix} \tag{27}$$

where $\frac{\partial \boldsymbol{f}^{\text{int}}}{\partial \boldsymbol{U}}=\boldsymbol{0}$, $\frac{\partial \boldsymbol{f}^{\text{int}}}{\partial \boldsymbol{P}}=\int_{\Gamma_\text{d}}[\![\boldsymbol{N}_\text{u}^\alpha]\!]^\text{T}\boldsymbol{n}_{\Gamma\text{d}}\boldsymbol{N}_\text{p}^\gamma d\Gamma$, $\frac{\partial \boldsymbol{q}^{\text{int}}}{\partial \boldsymbol{U}}=-\frac{a_2}{a_1\Delta t}\int_{\Gamma_\text{d}}\left(\boldsymbol{N}_\text{p}^\gamma\right)^\text{T}(\boldsymbol{n}_{\Gamma\text{d}})^\text{T}[\![\boldsymbol{N}_\text{u}^\alpha]\!]d\Gamma+\frac{a_2}{a_1\Delta t}\int_{\Gamma_\text{d}}w_\text{N}\left(\boldsymbol{N}_\text{p}^\gamma\right)^\text{T}(\boldsymbol{m}_{\Gamma\text{d}})^\text{T}\boldsymbol{m}_{\Gamma\text{d}}\langle\nabla\boldsymbol{N}_\text{u}^\alpha\rangle d\Gamma+\frac{1}{a_1\Delta t^2}\int_{\Gamma_\text{d}}k_\text{f}w_\text{N}\rho_\text{f}\left(\nabla\boldsymbol{N}_\text{p}^\gamma\right)^\text{T}(\boldsymbol{m}_{\Gamma\text{d}})^\text{T}\boldsymbol{m}_{\Gamma\text{d}}\langle\boldsymbol{N}_\text{u}^\alpha\rangle d\Gamma$, and $\frac{\partial \boldsymbol{q}^{\text{int}}}{\partial \boldsymbol{P}}=\int_{\Gamma_\text{d}}k_\text{f}w_\text{N}\left(\nabla\boldsymbol{N}_\text{p}^\gamma\right)^T(\boldsymbol{m}_{\Gamma\text{d}})^T\boldsymbol{m}_{\Gamma\text{d}}\nabla\boldsymbol{N}_\text{p}^\delta d\Gamma+\frac{1}{b_1\Delta t}\int_{\Gamma_\text{d}}w_\text{N}\left(\boldsymbol{N}_\text{p}^\gamma\right)^T\boldsymbol{N}_\text{p}^\delta/K_\text{f}d\Gamma$.

During time step t_{n+1}, the increments of displacement and pressure at the i-th iteration step are obtained from:

$$\begin{bmatrix} d\mathbf{U}_{n+1} \\ d\mathbf{P}_{n+1} \end{bmatrix}^{i+1}=-\begin{bmatrix} \mathbf{R}_{n+1}^\text{u} \\ \mathbf{R}_{n+1}^\text{p} \end{bmatrix}^{i}\cdot\left(\mathbf{J}_{n+1}^i\right)^{-1} \tag{28}$$

The Jacobian matrix requires updating at every iteration to account for fracture aperture evolution, and the iterative procedure continues until the convergence criterion $\|\, d\mathbf{U}_{n+1} \quad d\mathbf{P}_{n+1}\,\|^i / \|\,\mathbf{U}_{n+1} \quad \mathbf{P}_{n+1}\,\|^i < 10^{-6}$ is satisfied.

This process describes the solution for displacement and pore pressure within one time step. The full simulation comprises two sequential stages: EE followed by hydraulic fracturing, as illustrated in Fig. 2. Upon completion of the EE calculation, the computed stress and displacement fields serve as the initial conditions for the hydraulic fracturing simulation. Both stages employ the Newton–Raphson method to solve the coupled u-p coupled equations as presented above. Critically, fracture propagation is modeled only during hydraulic fracturing, while fractures are not considered in the EE stage.

4. Numerical results

4.1. Verification of the hydraulic fracturing in porous media

To validate the accuracy of the proposed XFEM-based fully coupled enhanced-fracturing model, we benchmarked it against the classical Khristianovich-Geertsma-de Klerk (KGD) problem for HF propagation in porous media. Considering the geometric symmetry of the KGD configuration, we reduced computational costs by analyzing only half of the domain (Fig. 3). The model's left boundary was fixed in the horizontal direction ($u_x = 0$), while vertical displacement at the midpoint of the right boundary was constrained ($u_y = 0$). In-situ stress conditions were replicated by applying 4 MPa minimum horizontal stress to the top and bottom boundaries and 6 MPa maximum horizontal stress to the right boundary. Initial pore pressure throughout the domain was set to zero, with zero-pressure boundaries imposed on all sides except the impermeable left boundary ($q = 0$), a condition consistent with the symmetry requirements. A pre-existing horizontal fracture (initial length 0.05 m) was initialized at the left boundary midpoint, with Newtonian fluid injected at a constant flow rate Q to drive its propagation.

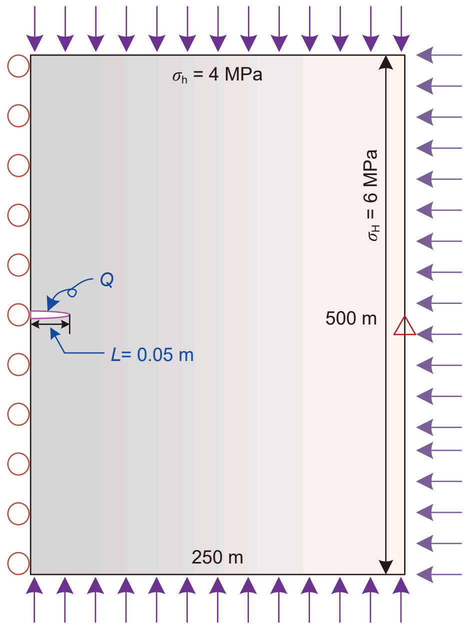

Fig. 3. Computational model.

Hydraulic fracture propagation in permeable media was investigated by Hu and Garagash (2010), who identified four distinct regimes through dimensionless toughness (K_m) and dimensionless leak-off (C_m) coefficients. These propagation regimes consist of four limiting scenarios: viscosity-storage-dominated ($K_m = 0$, $C_m = 0$), toughness-storage-dominated ($K_m \to \infty$, $C_m = 0$), viscosity-leak-off-dominated ($K_m = 0$, $C_m \to \infty$), and toughness-leak-off-dominated ($K_m \to \infty$, $C_m \to \infty$). According to Detournay (2004) and Adachi and Detournay (2008), the expressions of K_m and C_m are defined as:

$$\begin{cases} K_m = K'\left(\dfrac{1}{E'^3\mu' Q'}\right)^{\frac{1}{4}} \\ C_m = C'\left(\dfrac{E't}{\mu' Q'^3}\right)^{\frac{1}{6}} \end{cases} \tag{29}$$

where $K' = 4K_{Ic}\sqrt{\frac{2}{\pi}}$, $E' = \frac{E}{1-\nu^2}$, $\mu' = 12\mu$, and $Q' = 2Q$. Detournay (2004) demonstrated that critical thresholds of K_m govern fracture mechanics: when $K_m < 1$, viscous dissipation dominates fracture evolution, whereas $K_m > 4$ indicates that most energy is expended in new fracture creation. To comprehensively validate the computational model, three numerical cases (Table 2) were designed with progressively reduced matrix permeability (1, 0.1, and 0.01 mD) to isolate leak-off effects. This permeability reduction strategy systematically minimized fluid infiltration into the rock matrix, enabling controlled comparisons with analytical solutions. As permeability decreased, Case 1 was designed to approach the near-*K*-vertex solution ($K_m = 4$ and $C_m \approx 0$), Case 2 was configured to converge toward the near-*M*-vertex solution ($K_m = 1$ and $C_m \approx 0$), and Case 3 was structured to investigate transitional behavior near the *MK*-edge solution ($K_m = 3$ and $C_m \approx 0$).

Hu and Garagash (2010) established analytical solutions for hydraulic fracturing in permeable media based on the dimensionless toughness and leak-off coefficients. These solutions explicitly describe the temporal evolution of injection pressure, fracture length, and fracture aperture at the injection point, governed by the relationship:

$$\begin{cases} w(0,t) = \Omega(0)L_m\varepsilon_m \\ p(0,t) = \Pi(0)E'\varepsilon_m \\ L(t) = \gamma L_m \end{cases} \tag{30}$$

where $L_m = \left(\frac{Q'^3E't^4}{\mu'}\right)^{\frac{1}{6}}$, $\varepsilon_m = \left(\frac{\mu'}{E't}\right)^{\frac{1}{3}}$, $w(0,t)$ denotes the injection-point aperture at time t, $p(0,t)$ represents the corresponding injection pressure, and $L(t)$ is the fracture length. The coefficients $\Omega(0)$, $\Pi(0)$, and γ in Eq. (30) depend on the values of K_m and C_m. Hu and Garagash (2010) quantified these coefficients for three characteristic scenarios: Near-*K*-vertex ($K_m = 4$, $C_m = 0.01$), Near-*M*-vertex ($K_m = 1$, $C_m = 0.01$), and *MK*-edge transition ($K_m = 3$, $C_m = 0.01$), as summarized in Table 3.

Fig. 4 presents a systematic validation of the computational model against analytical benchmarks across three distinct hydraulic fracturing regimes. In Case 1 (Fig. 4(a)–(c)), numerical results under matrix permeabilities of 1, 0.1, and 0.01 mD demonstrate that decreasing permeability enhances fracturing efficiency, as evidenced by progressive increases in fracture aperture and length. At 0.01 mD permeability, numerical results for fracture aperture and length align closely with the analytical solutions (solid black lines), confirming model accuracy under toughness-storage-dominated regimes. Fig. 4(d)–(f) compare numerical results from Case 2 against near-*M*-vertex solutions ($K_m = 1$ and $C_m = 0.01$). The high fracturing fluid viscosity (0.1 Pa·s) minimizes leak-off effects, resulting in numerical results that closely match the analytical solution. A marginal increase in fracture aperture and improved convergence to analytical solutions are observed as matrix permeability decreases. This trend continues in Case 3 (Fig. 4(g)–(i)), where reduced permeability enhances aperture, fracture length, and efficiency while reducing fluid loss. The results converge to transitional regime benchmarks ($K_m = 3$ and $C_m = 0.01$), validating the model's ability to capture intermediate behaviors. Notably, simulated injection pressures in all cases (Fig. 4(a), (d) and (g)) exceed analytical solutions—a

Table 2
Input parameters for model validation.

Input parameters	Symbol	Case 1	Case 2	Case 3
Fluid viscosity, mPa·s	μ	1	100	6
Injection rate, m^2/s	Q	1×10^{-4}	1.25×10^{-4}	1.25×10^{-4}
Fracture toughness, $MPa{\cdot}m^{0.5}$	K_{IC}	2.5	2	3
Dimensionless toughness, -	K_m	4.17	0.9991	3.0281
Young's modulus, GPa	E	17		
Poisson's ratio, -	ν	0.2		
Biot Coefficient, -	α	1		
Porosity, %	ϕ	12		
Solid density, kg/m^3	ρ_s	2000		
Fluid density, kg/m^3	ρ_f	1000		
Bulk modulus of Solid, GPa	K_s	36		
Bulk modulus of fluid, GPa	K_f	3		
Matrix permeability, mD	k_m	1、0.1、0.01		

Table 3
Parameters of analytical solutions.

Regime type	Near-*K*-vertex	Near-*M*-vertex	Near-*MK*-edge
Validation case	Case 1	Case 2	Case 3
Dimensionless toughness K_m	4	1	3
Dimensionless leak-off C_m	0.01	0.01	0.01
$\Omega(0)$	1.7429	1.1388	1.4776
$\Pi(0)$	1.2094	0.5589	0.8791
γ	0.36439	0.59122	0.43024

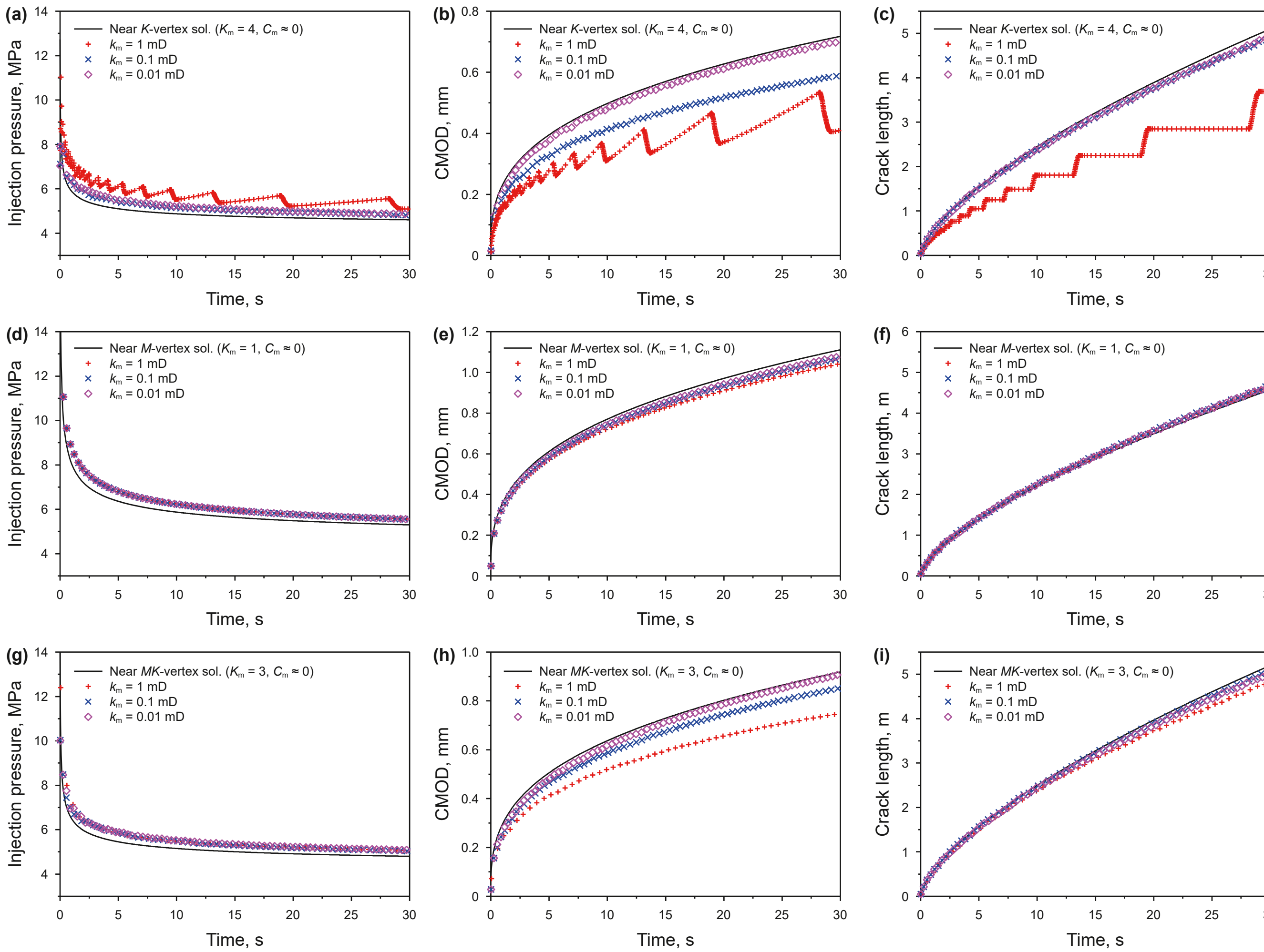

Fig. 4. Comparison between analytical solutions and numerical results under different matrix permeability: (**a**)–(**c**) injection pressure, crack mouth opening displacement (CMOD), and fracture length for Case 1; (**d**)–(**f**) injection pressure, CMOD, and fracture length for Case 2; (**g**)–(**i**) injection pressure, CMOD, and fracture length for Case 3 ($K_m = 3$).

discrepancy attributed to pore pressure elevation and localized stress amplification from hydro-mechanical coupling. This phenomenon aligns with findings reported by other fully coupled models (Carrier and Granet, 2012; Paul et al., 2018). These results collectively validate the model's ability to simulate hydraulic fracture propagation across different regimes.

4.2. Influence of energy enhancement on hydraulic fracturing

4.2.1. Model set-up

The computational model is shown in Fig. 5, where the formation pressure is first increased by injecting energy-enhancing fluid at the center of a 500 m × 500 m reservoir domain for a duration of T_{EE}. Subsequently, hydraulic fracturing is conducted either at the energy-enhanced injection point or at other designated locations. A maximum horizontal stress of $\sigma_H = 27.2$ MPa is applied along the left and right boundaries, with vertical displacement constraints imposed at their midpoints. Similarly, a minimum horizontal stress of $\sigma_h = 23.9$ MPa is applied to the top and bottom boundaries, with horizontal displacement constrained at their centers. A constant pore pressure of 8.5 MPa is maintained along all outer boundaries, consistent with the initial formation pressure conditions. This section investigates the effects of stress

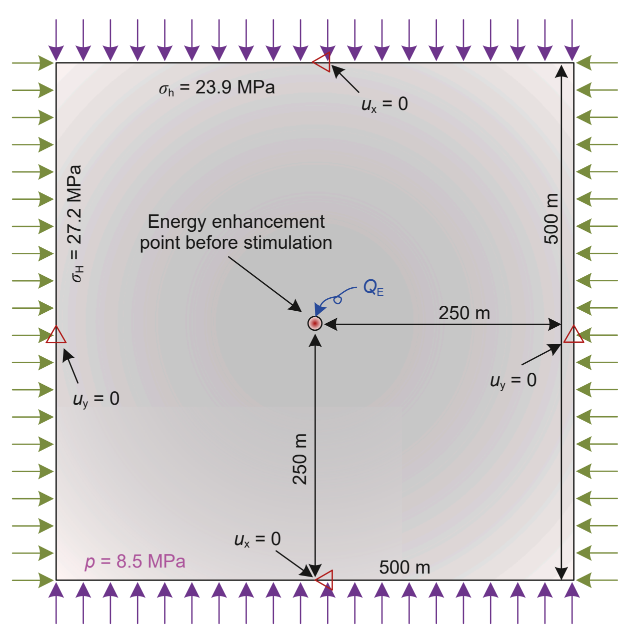

Fig. 5. Computational model.

Table 4
Input parameters for parameter sensitivity analysis.

Parameter of energy enhancement process			
	Influencing factors	Symbol	Value
Case 1	Formation permeability, mD	k_m	0.2–5
Case 2	Energy-enhanced volume, day	T_{EE}	0–30
Case 3	Energy-enhanced rate, m^2/s	Q_{EE}	(1–5)×10^{-5}
Case 4	Energy-enhanced viscosity, mPa·s	μ_{EE}	0.1–2
Case 5	Shut-in time, day	T_{SI}	0–30
Case 6	Fracture initiation location, m	d	0–50
	Fracture initiation orientation, °	θ_f	0–90°

Table 5
Other parameters for parameter sensitivity analysis.

Input parameters	Symbol	Value
Young's modulus, GPa	E	28
Poisson's ratio, -	ν	0.3
Matrix permeability, mD	k_m	1
Energy-enhanced time, day	T_{EE}	30
Energy-enhanced rate, m^2/s	Q_{EE}	3×10^{-5}
Fluid viscosity of EE, mPa·s	μ_{EE}	1
Biot Coefficient, -	α	1
Porosity, %	ϕ	12
Solid density, kg/m^3	ρ_s	2000
Fluid density, kg/m^3	ρ_f	1000
Bulk modulus of Solid, GPa	K_s	36
Bulk modulus of fluid, GPa	K_f	3
Fluid viscosity of HF, mPa·s	μ_{HF}	5
Injection rate of HF, m^2/s	Q_{HF}	10^{-3}
Fracture Toughness, MPa·m$^{0.5}$	K_{Ic}	1.5

and pressure changes on the subsequent propagation of HF. The analysis focuses on several key parameters, including formation permeability, energy-enhanced volume, energy-enhanced rate, energy-enhanced fluid viscosity, shut-in time after EE, and the location of fracture initiation. The parameters used for sensitivity analysis and hydraulic fracturing simulations are provided in Table 4. Unless otherwise specified, all other material and input parameters are listed in Table 5.

4.2.2. Formation permeability

This section examines the influence of reservoir permeability on HF propagation following energy-enhanced injection, aiming to evaluate the sensitivity of fracturing performance to the energy-enhanced treatment and to identify conditions under which EE exerts negligible influence. Water serves as the energy-enhanced fluid, with an injection rate $Q_{EE} = 3 \times 10^{-5}$ m^2/s (2.61 m^3/(m·day)) applied over $T_{EE} = 30$ days. Five different reservoir permeability values ($k_m = 0.2$, 0.5, 1, 2, and 5 mD) are considered and compared to corresponding non-EE cases under identical permeability conditions. In all cases, HFs initiate from the center of the model domain, and the input parameters are listed in Tables 4 and 5

The evolution of reservoir stress and pressure during energy enhancement plays a critical role in governing the subsequent propagation of HF. Since the parametric variations primarily influence the magnitude of responses rather than the underlying physical mechanisms, this section employs a baseline case to investigate the effect of energy enhancement on the variations in formation pressure and stress. Accordingly, the following sections focus on the effects of EE on fracture propagation behavior, and the associated stress and pressure field evolution is not discussed further.

(a) Influence of EE on formation pressure and stress

Fig. 6(a) shows the spatial distribution of pressure along the X-axis after 30 days of EE under different matrix permeabilities. The use of a single-point injection method results in a pressure singularity at the injection point—an effect analogous to concentrated mechanical loading. This singularity generates unrealistically high-pressure values that escalate with mesh refinement, making them unsuitable for evaluating EE performance. To eliminate mesh dependency, the analysis employs the average pressure within a defined radius around the injection point. Fig. 6(b) tracks the temporal evolution of the average pressure within a 25-m radius under varying matrix permeabilities. The results indicate that pressure near the injection point increases rapidly at first, then gradually approaches a steady state as fluid continues to enter the formation. Lower permeability

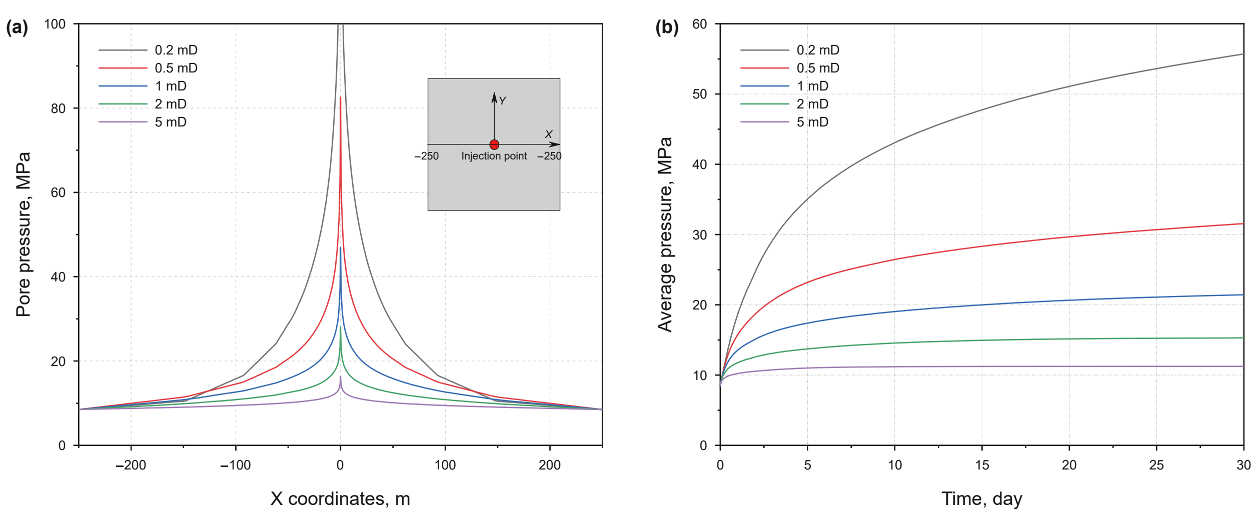

Fig. 6. Numerical results of pressure evolution: (**a**) pressure profile along the X-axis; (**b**) temporal variation of average pressure within a 25 m radius of the injection point.

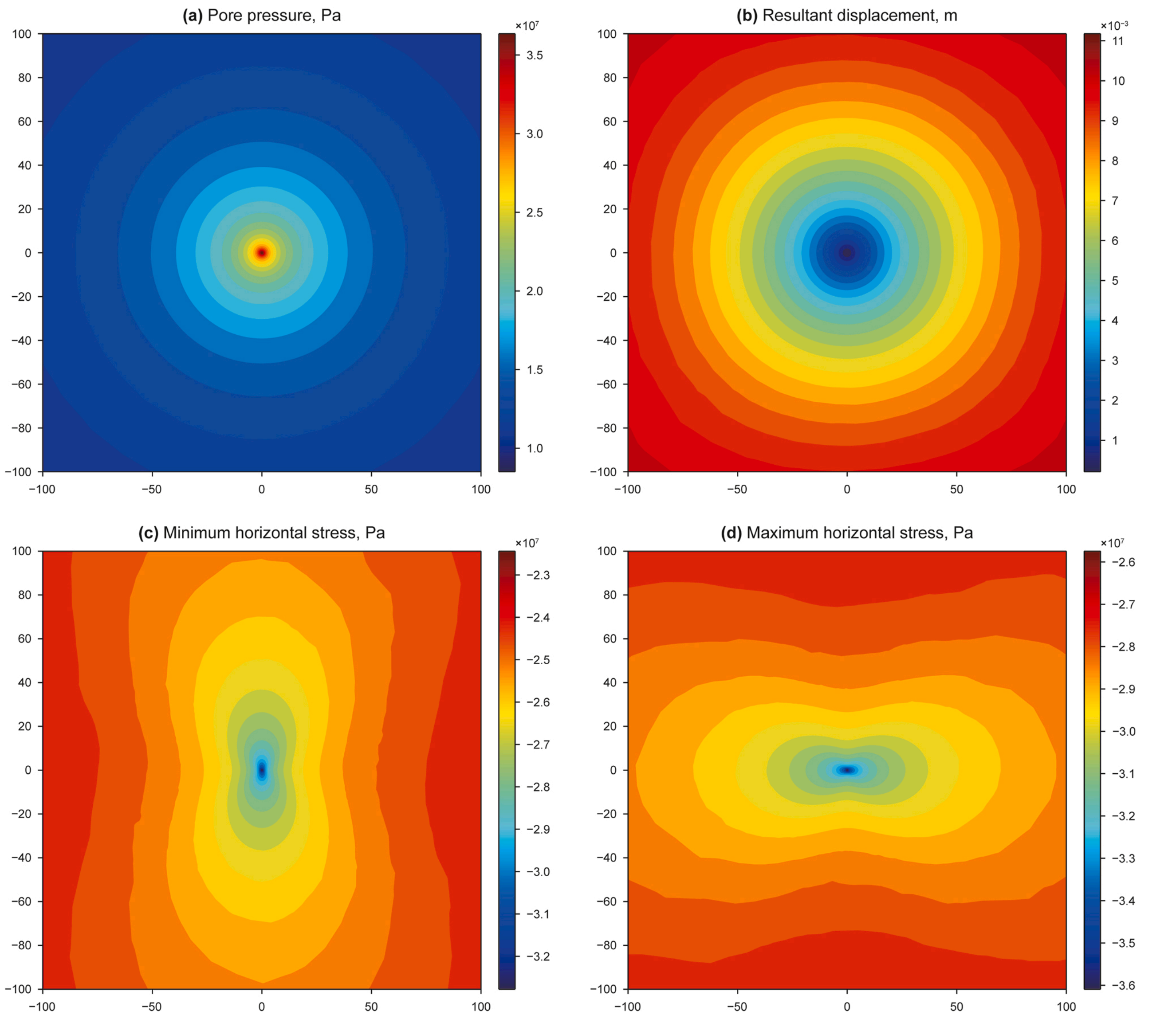

Fig. 7. Simulation results after 30 days of EE in a 1 mD formation: (**a**) pressure contours; (**b**) total displacement contours; (**c**) total minimum horizontal stress; (**d**) total maximum horizontal stress contours.

results in a more rapid and pronounced pressure buildup. For instance, a formation with 0.5 mD permeability exhibits accelerated pressurization, reaching 31.5 MPa after 30 days—three times the 11.23 MPa observed in the case of 5 mD permeability. Fig. 7(a) presents the pressure contours after 30 days of injection for a formation with 1 mD permeability. As shown, pressure peaks at the injection point and decreases outward, forming concentric contours that confirm radial flow symmetry. Fig. 7(b) shows the corresponding displacement field induced by 30 days of EE. Displacements increase radially and reach their maximum at the domain boundaries, while maintaining circular symmetry that aligns with the pressure distribution. The consistent pressure and displacement distributions confirm the hydro-mechanical coupling governing reservoir deformation during EE.

Fig. 7(c) and (d) present the distributions of total minimum and maximum horizontal stress, respectively, after 30 days of EE in a low-permeability (1 mD) reservoir. The results show that hydro–mechanical coupling transforms the initially uniform in-situ stress field into a heterogeneous one. Near the injection point, the maximum magnitude of σ_h increases from 23.9 MPa to approximately 32.6 MPa, while the maximum magnitude of σ_H rises from 27.2 MPa to about 36 MPa. These changes indicate that both the maximum and minimum horizontal stresses increase concurrently, with the stress difference remaining nearly constant during EE. Spatially, minimum horizontal stress forms a figure-eight shape, while the maximum horizontal stress resembles an infinity symbol, with both gradients decaying radially outward. Total minimum horizontal stress intensifies directly above and below the injection points but diminishes rapidly with lateral distance. In contrast, maximum horizontal stress increments are most pronounced along the lateral direction and decrease quickly along the vertical axis, returning to far-field stress. Overall, numerical results in Figs. 6 and 7 demonstrate that lower matrix permeability leads to higher pore pressure accumulation and steeper pressure gradients. These effects enhance the seepage forces, strengthen hydro–mechanical coupling, and intensify stress rotation. In extreme cases, this may lead to stress reversal, which can significantly influence HF propagation.

Fig. 8 presents the evolution of maximum (σ_H) and minimum (σ_h) horizontal stress orientations after 30 days of energy-

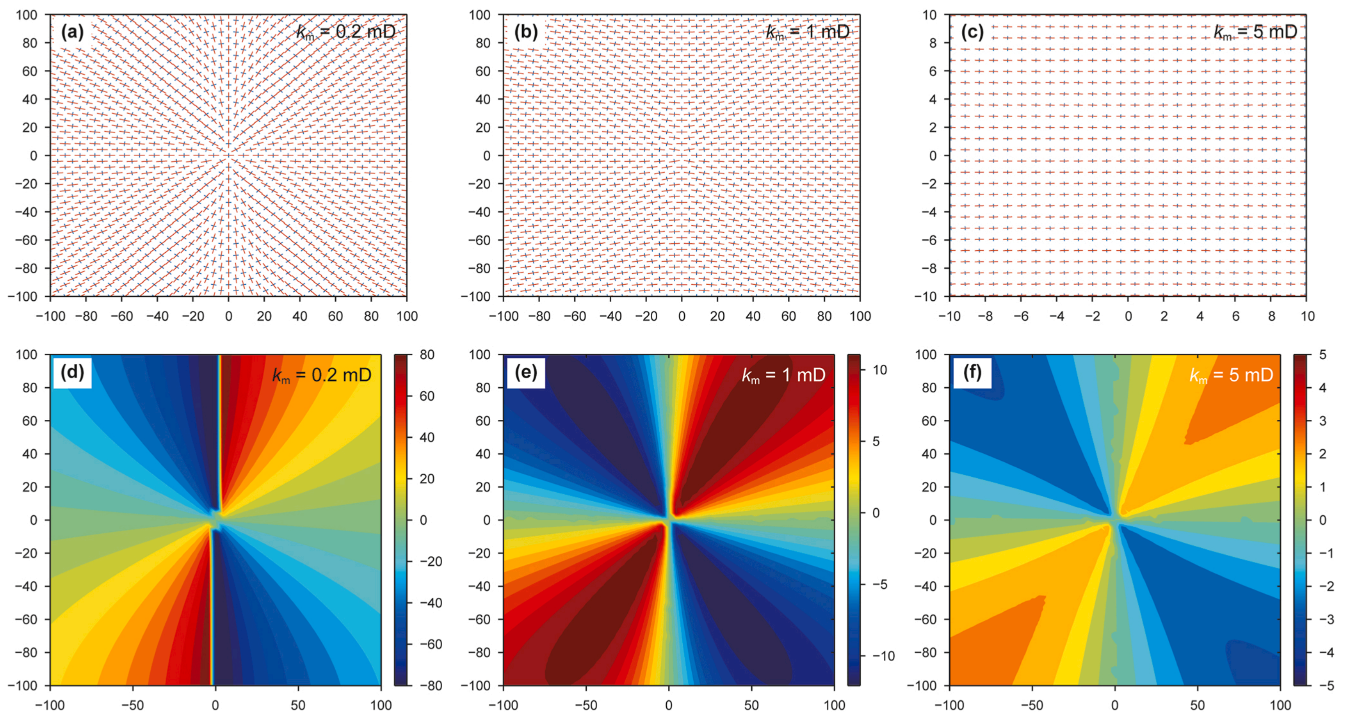

Fig. 8. Horizontal principal stress orientations and deflection angles after 30 days of energy-enhanced injection in formations with different matrix permeabilities: (**a**)–(**c**) horizontal principal stress orientations for $k_m = 0.2$ mD/1 mD/5 mD; (**d**)–(**f**) corresponding deflection angles of principal stress. Note: Blue lines indicate the direction of σ_h; Red vectors indicate the direction of the σ_H. Deflection sign convention: Positive for counterclockwise and negative for clockwise rotation relative to the initial orientation.

enhanced injection across formations with varying matrix permeabilities. In Fig. 8(a)–(c), compressive stress is defined as positive, with σ_H and σ_h orientations represented by long red and short blue lines, respectively. Prior to injection, the stress field is uniform, with σ_H oriented horizontally and σ_h vertically. As shown in Fig. 8(a), in low-permeability formation (0.2 mD), significant stress rotation (>80°) occurs vertically above and below the injection point ($x = 0$ m), where σ_H becomes nearly vertical due to increased minimum horizontal stress. In contrast, stress orientations remain largely unchanged along the lateral direction (near $y = 0$). This pattern is confirmed by the deflection contour in Fig. 8(d), which shows that the greatest rotation of σ_H occurs near $x = 0$ m, exceeding 80°, while deflections near $y = 0$ m are minimal. As matrix permeability increases to $k_m = 1$ mD, the degree of stress rotation decreases (Fig. 8(b)). Fig. 8(e) illustrates that the maximum deflection of σ_H is concentrated along the 45° and 135° directions, reaching approximately 13°. At higher permeability ($k_m = 5$ mD), the principal stress orientations remain nearly unchanged from their initial state after EE, as shown in Fig. 8(c). The corresponding deflection contour in Fig. 8(f) shows only minor rotation, with a maximum angle of just 2.6°, again concentrated along the 45° and 135° directions.

(b) Influence of EE on hydraulic fracturing

Fig. 9(a) shows the evolution of injection pressure during hydraulic fracturing following 30 days of energy-enhanced injection in reservoirs with varying permeability. Numerical results indicate that lower-permeability formations require significantly higher fracture initiation and propagation pressures. When reservoir

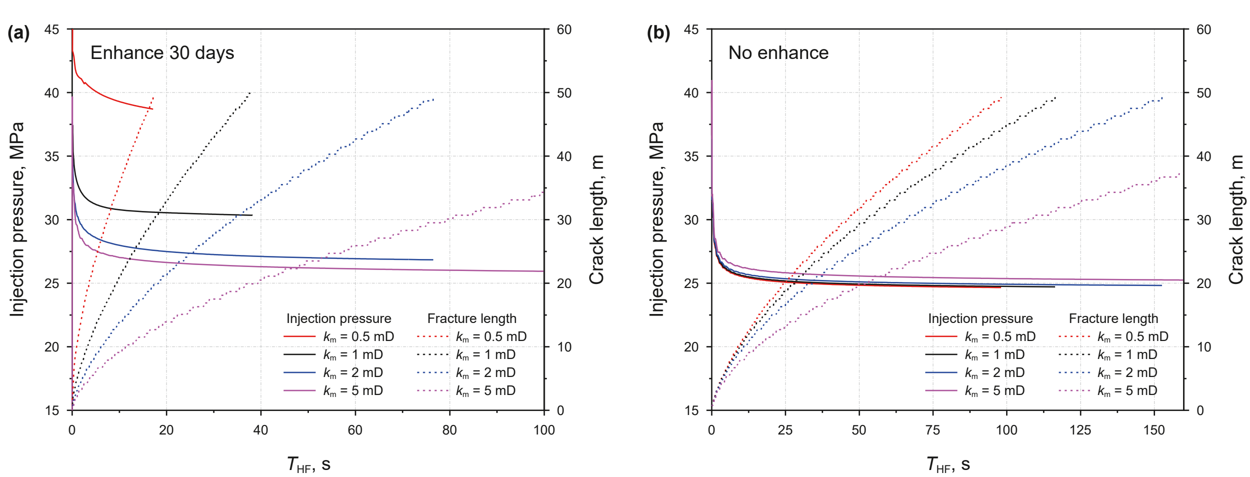

Fig. 9. Temporal evolution of injection pressure and fracture length for different k_m: (**a**) hydraulic fracturing with 30-day EE; (**b**) hydraulic fracturing without EE.

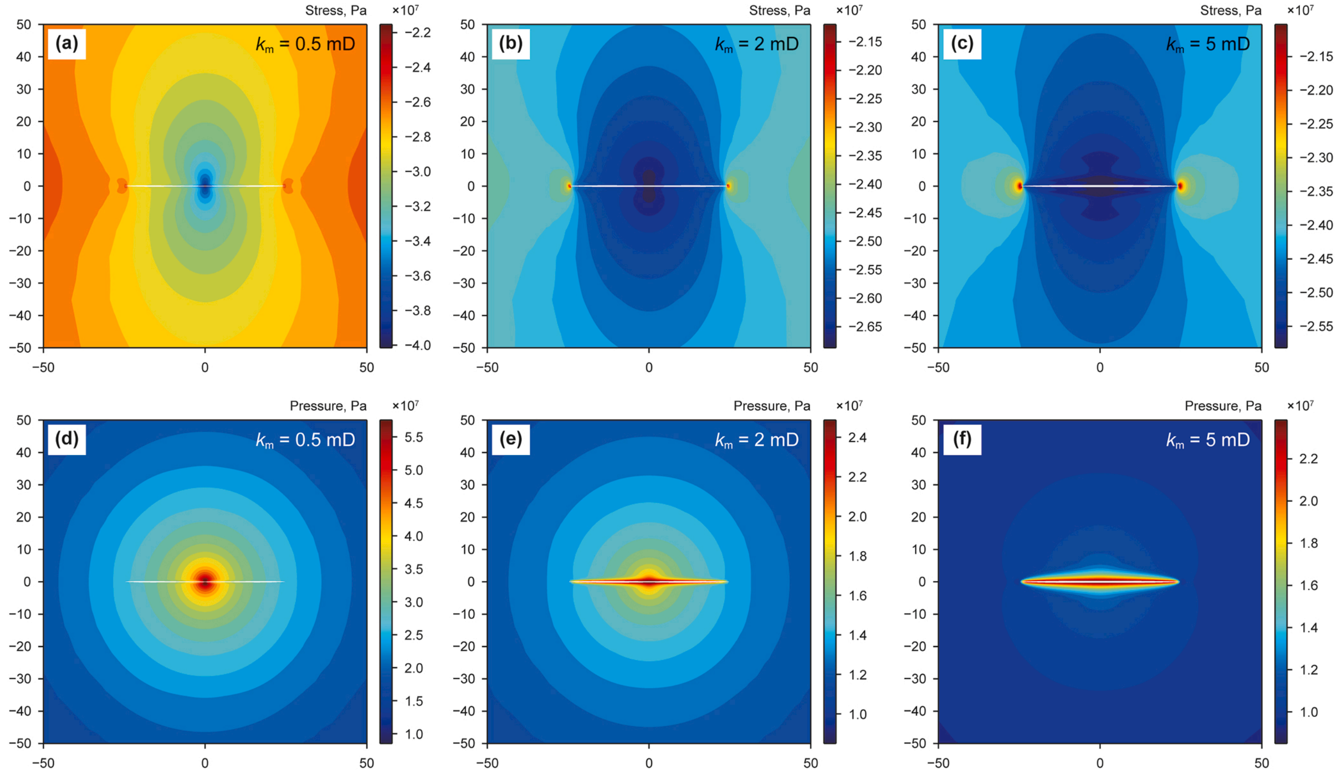

Fig. 10. Numerical results of stress and pressure when $L_{HF} = 50$ m: (**a**)–(**c**) minimum horizontal stress with $k_m = 0.5$ mD, $k_m = 2$ mD, and $k_m = 5$ mD; (**d**)–(**f**) pore pressure with $k_m = 0.5$ mD, $k_m = 2$ mD, and $k_m = 5$ mD.

permeability decreases from 5 mD to 0.5 mD, the fracture propagation pressure after 30 days of EE increases from 25.82 MPa to 38.70 MPa at $L_{HF} = 50$ m. In comparison, Fig. 9(b) shows that the propagation pressures for the corresponding permeabilities without EE are 25.14 MPa and 24.66 MPa, respectively. In the 0.5 mD reservoir, EE increases the propagation pressure by more than 14 MPa compared to the non-EE case. By contrast, in the 5 mD reservoir, the injection pressure remains virtually unchanged before and after EE, with only a minor difference observed when the fracture length reaches 50 m. These results demonstrate that the influence of pre-fracturing EE on subsequent fracture propagation diminishes as permeability increases, becoming negligible when permeability exceeds 5 mD under the studied conditions. Fracture length evolution further demonstrates this permeability control mechanism. In non-EE cases (Fig. 9(b)), permeability variations primarily change fluid leak-off rates, resulting in distinct fracture lengths (11.5–17.5 m at 20 s) despite similar injection pressure curves. However, Fig. 9(a) shows that EE leads to greater variations in fracture length (13.9–52 m at 20 s) across different permeabilities compared to the non-EE cases. This suggests that the variation in fracture length after EE across different matrix permeabilities is the combined result of permeability-dependent leak-off and formation pressure changes induced by EE.

Fig. 10 shows the pressure and minimum horizontal stress distributions when the fracture length reaches 50 m after 30 days of energy-enhanced injection in reservoirs with different permeabilities. In the low-permeability case ($k_m = 0.5$ mD), high pressures are concentrated near the injection point. Although the average pressure along the HF approaches 30 MPa, it remains below the surrounding formation pressure near the injection point. At a permeability of 2 mD, the average fracture pressure (25.9 MPa) is nearly equal to the peak formation pressure (28.05 MPa) near the injection location. However, when the permeability increases to 5 mD, the average pressure along the HF (25.3 MPa) exceeds the average formation pressure within 25 m of the injection point (11.23 MPa). These observations suggest that reservoir permeability controls the pore pressure gradient induced by EE, which in turn governs the evolution of the stress field. As shown in Fig. 10(a), in a low-permeability formations ($k_m = 0.5$ mD), the stress field is dominated by the seepage of energy-enhanced fluid, leading to a generally higher stress state. In contrast, when permeability increases to 5 mD, the stress field is minimally affected by energy-enhanced injection and is instead largely shaped by the subsequent fracturing process. This trend is further reflected in the fracture aperture distributions shown in Fig. 11. At a permeability of 0.5 mD, the fracture aperture at the injection point is further reduced to 0.179 mm, smaller than that in the 1 mD case (0.318 mm). In contrast, at 5 mD, the aperture displays an elliptical shape, closely resembling the non-EE case, implying that the effects of EE have largely dissipated. Overall, the simulation results demonstrate that lower permeability reservoirs experience greater stress field modification due to EE, which significantly impacts subsequent fracture propagation. As

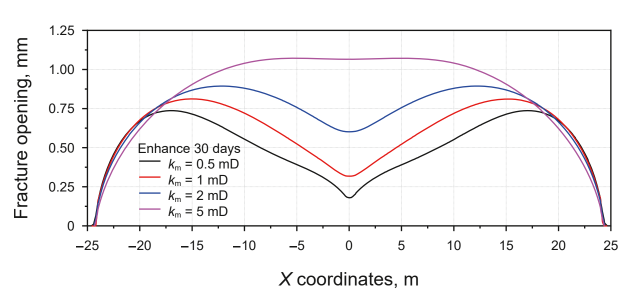

Fig. 11. Fracture aperture distributions for different k_m when $L_{HF} = 50$ m.

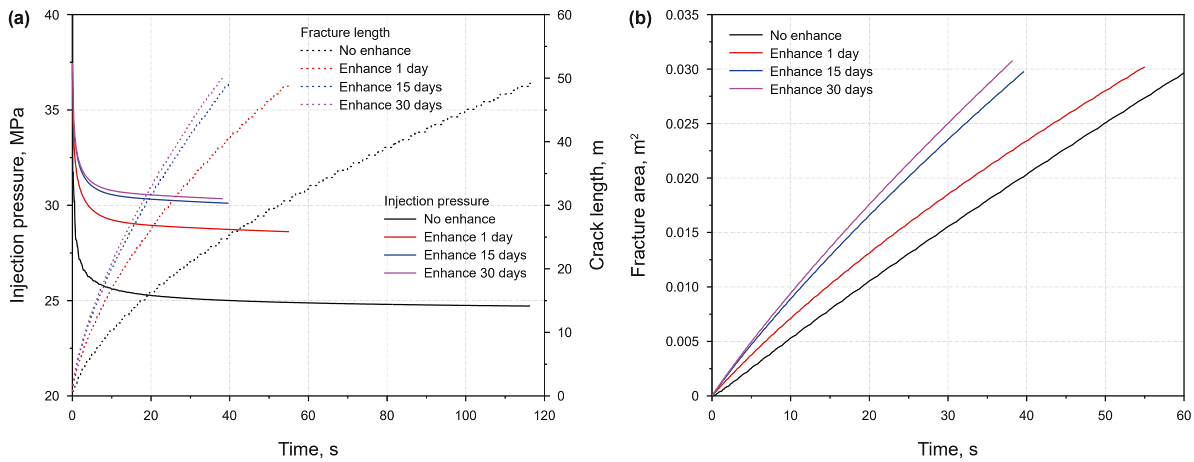

Fig. 12. Temporal evolution of HF propagation under different T_{EE}: (**a**) injection pressure and fracture length; (**b**) fracture area.

permeability increases, this effect weakens, and the role of EE becomes negligible.

4.2.3. Energy-enhanced injection volume

This section examines how the volume of energy-enhanced fluid injected prior to hydraulic fracturing affects subsequent propagation of HF. Since the energy-enhanced rate (Q_{EE}) remains constant, the injection duration (T_{EE}) serves as the primary control variable for quantifying this effect. As detailed in Table 4, water was selected as the energy-enhanced fluid, with a reservoir permeability of 1 mD and an injection rate of 3×10^{-5} m^2/s (2.6 $m^3/(m \cdot day)$). Five distinct injection durations ($T_{EE} = 0$, 0.1, 1, 15, and 30 days) were implemented to investigate the influence of T_{EE} on HF propagation. Hydraulic fractures were initiated at the energy-enhanced injection point, where a horizontal fracture with negligible initial length was pre-defined following EE. The subsequent fracturing operation employed a fluid with a viscosity of 5 mPa·s, injected at a rate of 10^{-3} m^2/s (Q_{HF}), into rock with a fracture toughness of 1.5 MPa·$m^{0.5}$. The input parameters are listed in Tables 4 and 5

Fig. 12(a) illustrates the evolution of injection pressure and fracture length over time during hydraulic fracturing for five different cases ($T_{EE} = 0$, 0.1, 1, 15, and 30 days). In all cases, the fracturing fluid injection continued until the fracture length reached 50 m. As T_{EE} increases, both HF initiation pressure and propagation pressure rise. However, the rate of increase diminishes with longer T_{EE}. Specifically, the propagation pressure increases from 24.71 MPa in the baseline case (no EE) to 28.6 MPa (1-day EE), 30.1 MPa (15-day EE), and 30.3 MPa (30-day EE). The marginal increase of 0.2 MPa between the 15-day and 30-day cases is significantly smaller than the 5.1 MPa rise observed from 0 to 15 days. The increase in injection pressure is attributed to the increase in minimum horizontal principal stress near the injection point along the horizontal axis ($y = 0$), as shown in Fig. 13(a)–(d). The resulting minimum horizontal stress elevation requires a higher injection pressure to drive HF propagation.

Fracture length evolution also reflects the impact of energy-enhanced injection. As shown in Fig. 12(a), longer T_{EE} results in longer fractures at the same fracturing time. After 40 s of injection, the fracture extends 25.3 m without EE, compared to 40.3, 49.3,

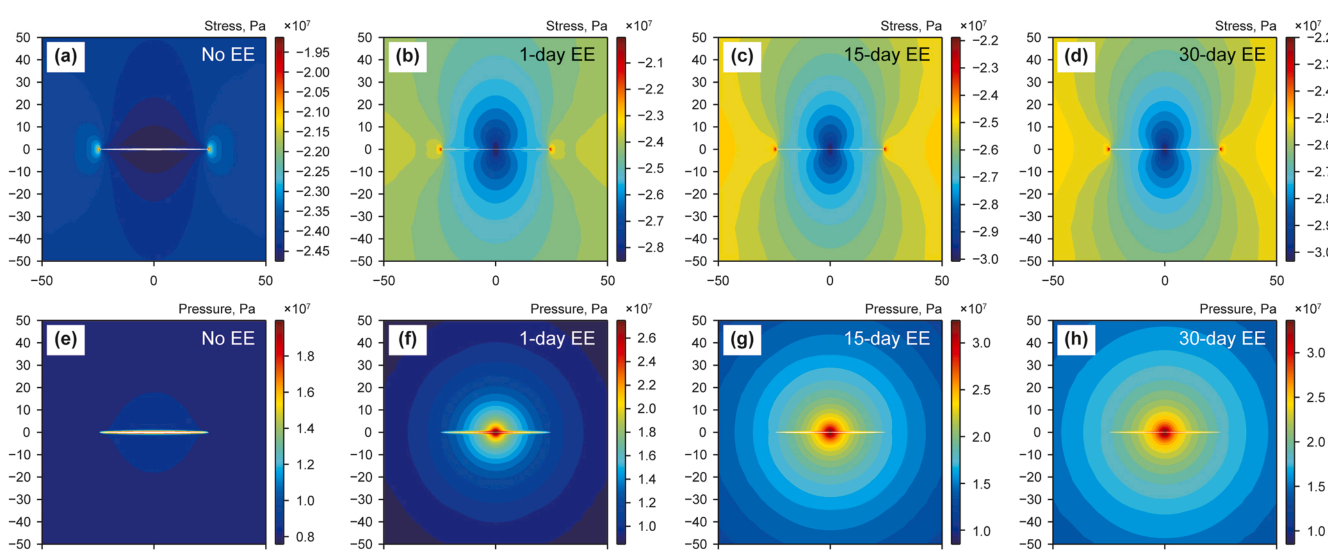

Fig. 13. Numerical results of stress and pressure when $L_{HF} = 50$ m: (**a**)–(**d**) minimum horizontal stress for no EE, 1-day EE, 15-day EE, and 30-day EE; (**e**)–(**h**) pore pressure for the corresponding cases.

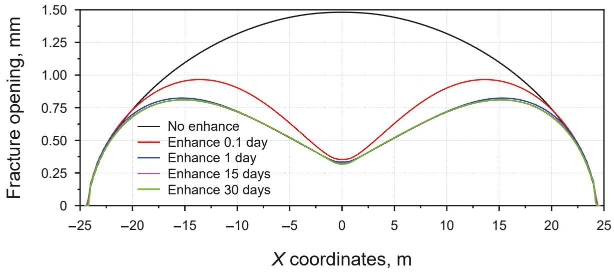

Fig. 14. Fracture aperture distributions for different T_{EE} when $L_{HF} = 50$ m.

and 49.9 m after 1, 15, and 30 days of EE, respectively. This effect is primarily induced by larger injection volumes (Fig. 13(e)–(h)), which reduces the pressure differential between the fracturing fluid and the formation, thereby improving fracturing efficiency. This enhancement is further supported by Fig. 12(b), which shows an increase in fracture area from 0.02 m^2 (no EE) to 0.03 m^2 (15-day EE). Correspondingly, fracturing efficiency rises from 50% to 75%, indicating a substantial improvement in hydraulic fracturing performance with increasing T_{EE}.

Fig. 14 illustrates the impact of energy-enhanced injection volumes on fracture aperture distribution after HFs propagate to a length of 50 m. Without energy enhancement, the aperture profile exhibits a classic elliptical shape. However, the energy-enhancement process significantly alters the fracture geometry, causing it to evolve into a saddle-shaped profile. This transformation is attributed to changes in the stress field near the injection point, where the minimum horizontal principal stress reaches its peak and gradually decreases radially outward, as shown in Fig. 13(a)–(d). Consequently, the fracture aperture at the injection point becomes a local minimum, decreasing from 1.5 mm in the baseline case to 0.318 mm after 30 days of EE. Simultaneously, the location of the maximum aperture, which remains below 1 mm, shifts approximately 15 m away from the initiation point. This reduction in aperture near the injection point may increase the risk of proppant bridging and screen-out, presenting potential operational challenges. Conversely, the elevated formation pressure associated with energy-enhanced injection reduces fluid leak-off, allowing greater fracture propagation under the same injection volume. Numerical results in this section underscore the dual effect of energy-enhanced injection, highlighting the importance of balancing increased formation pressure against the risk of near-wellbore flow restrictions to optimize hydraulic fracturing performance.

4.2.4. Energy-enhanced injection rate

This section investigates the influence of energy-enhanced injection rate on subsequent hydraulic fracture propagation. Water is used as the energy-enhanced fluid in all cases, with five different injection rates applied, ranging from $Q_{EE} = 1 \times 10^{-5}$ to 5×10^{-5} m^2/s per unit formation thickness, corresponding to 0.87–4.33 m^3/(m·day). To ensure a consistent total injection volume across all cases, the EE duration (T_{EE}) is adjusted to 90, 45, 30, 22.5, and 18 days, respectively. This results in a uniform cumulative injection volume of 78.3 m^3 per meter of formation thickness. Upon completion of the EE treatment, hydraulic fracturing is initiated at the injection point, followed by continued injection under standard fracturing conditions. The EE and fracturing parameters used in each case are listed in Tables 4 and 5.

Fig. 15(a) presents the temporal evolution of average formation pressure within a 25 m radius of the injection point and the corresponding cumulative injected volume during EE operations. Increasing the EE injection rate accelerates pressure buildup, resulting in higher terminal average pressures. For example, the average pressure rises from 13.06 MPa at $Q_{EE} = 0.87$ m^3/(m·day) to 28.4 MPa at $Q_{EE} = 4.33$ m^3/(m·day). This rapid pressure buildup occurs because limited fluid diffusion into the formation induces localized pore pressure accumulation near the wellbore. As shown in Fig. 15(b), these elevated pressures increase subsequent hydraulic fracturing pump pressures. After 90 days of EE at $Q_{EE} = 0.87$ m^3/(m·day), the fracture propagation pressure reaches 25.96 MPa, whereas 18-day EE at $Q_{EE} = 4.33$ m^3/(m·day) elevates it to 35.4 MPa—a 9.4 MPa increase. Furthermore, higher Q_{EE} drastically reduces fracture propagation time, shortening the duration to achieve a 50-m fracture length from 77 s ($Q_{EE} = 0.87$ m^3/(m·day)) to 20 s ($Q_{EE} = 4.33$ m^3/(m·day)).

Fig. 16 shows the pressure and stress distributions during the hydraulic fracturing state ($L_{HF} = 50$ m) following energy-enhanced injection of equivalent fluid volumes into reservoirs with different Q_{EE} values. As the energy-enhanced injection rate increases, the minimum horizontal stress induced by hydro-mechanical coupling becomes more significant, leading to higher injection pressures required to drive fracture propagation, as illustrated in Fig. 16(a)–(c). Meanwhile, the elevated formation pressure reduces the pressure differential between the fracturing fluid and the reservoir, thereby reducing fluid leak-off and

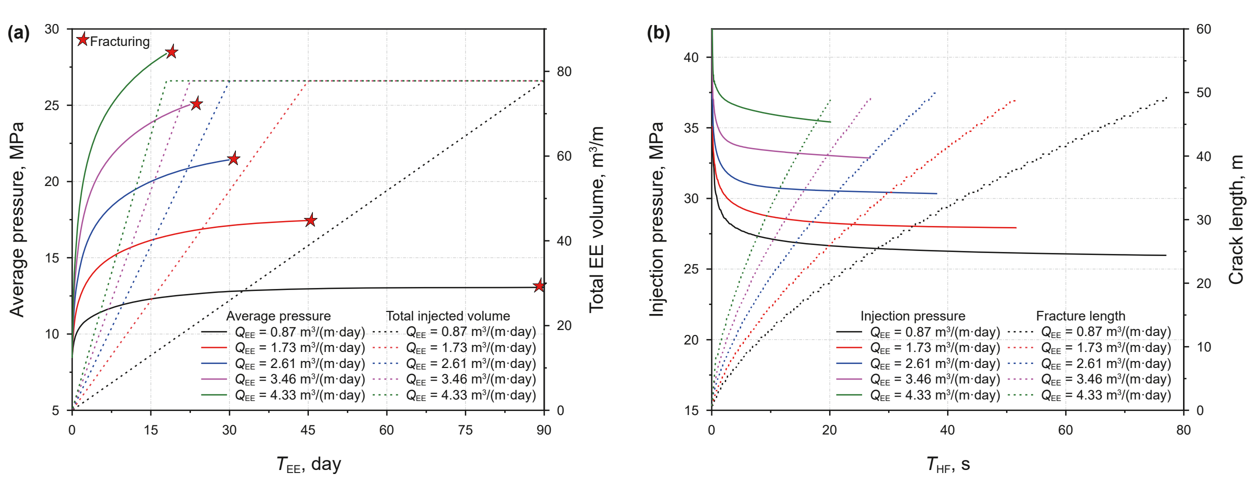

Fig. 15. Temporal evolution of key variables: (**a**) average pressure and total injected volume during EE; (**b**) injection pressure and fracture length during hydraulic fracturing.

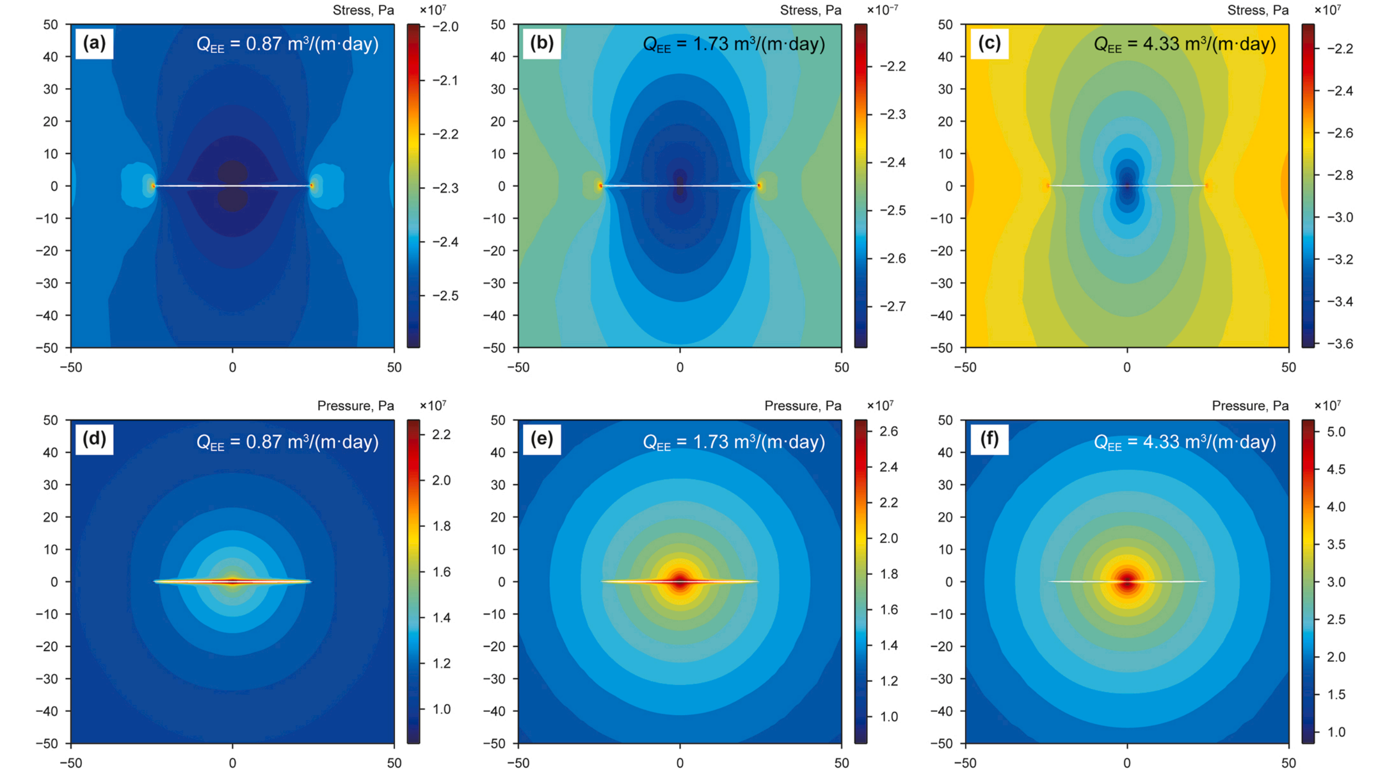

Fig. 16. Numerical results of stress and pressure when L_{HF} = 50 m: (**a**)–(**c**) minimum horizontal stress with Q_{EE} = 0.87, 1.73, and 4.33 m^3/(m·day); (**d**)–(**f**) pore pressure with Q_{EE} = 0.87, 1.73, and 4.33 m^3/(m·day).

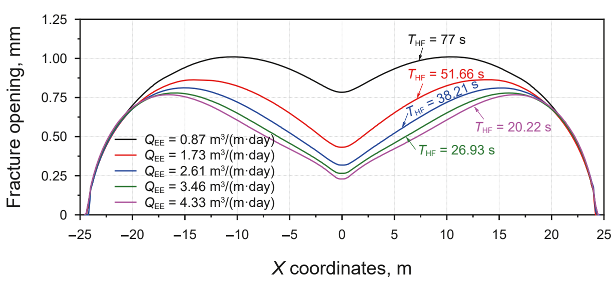

Fig. 17. Fracture aperture distributions for different Q_{EE} when L_{HF} = 50 m.

improving overall fracturing efficiency, as shown in Fig. 16(d)–(f). These effects are further supported by the fracture aperture profiles in Fig. 17. Under higher minimum horizontal stress, the fracture aperture at the injection point decreases from 0.784 mm (Q_{EE} = 0.87 m^3/(m·day)) to 0.229 mm (Q_{EE} = 4.33 m^3/(m·day)). In addition, Fig. 17 indicates that the final fracture areas are nearly identical across the three cases (Q_{EE} = 2.61, 3.46, and 4.33 m^3/(m·day)). However, the volumes of fracturing fluid injected per meter of formation thickness in these cases are 0.038, 0.0269, and 0.020 m^3, respectively. This suggests that higher Q_{EE} not only reduce injection time and fluid consumption but also sustain effective fracture propagation, demonstrating a more efficient stimulation process overall.

4.2.5. *Energy-enhanced fluid viscosity*

This section investigates the influence of energy-enhanced fluid viscosity on subsequent HF propagation. As detailed in Table 4, the reservoir permeability is set to 1 mD, with an injection rate of $Q_{EE} = 3 \times 10^{-5}$ m^2/s (2.61 m^3/(m·day)) applied over a duration of T_{EE} = 30 days. Four distinct energy-enhanced fluid viscosities (μ_{EE} = 0.1, 0.5, 1, and 2 mPa·s) were considered to investigate the influence of μ_{EE} on HF propagation. Upon completion of the EE treatment, hydraulic fracturing is initiated at the injection point, and the simulation is continued until the HF length reaches L_{HF} = 50 m. The EE and fracturing parameters used in each case are listed in Tables 4 and 5.

Fig. 18(a) presents the temporal evolution of the average formation pressure within a 25 m radius of the injection point and the corresponding cumulative injected volume during EE operations. Increasing the EE viscosity accelerates the pressure buildup, resulting in higher terminal average pressures. For example, the average pressure rises from 9.87 MPa at μ_{EE} = 0.1 mPa·s to 31.55 MPa at μ_{EE} = 2 mPa·s. As shown in Fig. 18(b), these elevated pressures also lead to an increase in subsequent hydraulic fracturing pumping pressures. Specifically, the propagation pressure increases from 24.71 MPa in the baseline case (no EE) to 25.05 MPa (0.1 mPa·s), 26.84 MPa (0.5 mPa·s), 30.34 MPa (1 mPa·s), and 38.05 MPa (2 mPa·s). The numerical simulation results indicate that a lower EE fluid viscosity leads to rapid diffusion within the formation, resulting in a relatively small change in pore pressure and consequently a limited influence on subsequent fracture propagation. In contrast, when the EE fluid viscosity increases to 2 mPa·s, its migration velocity is significantly reduced, resulting in a notable increase in both the pore pressure and the total stress near the injection well, as illustrated in Fig. 19. This pressure accumulation leads to a markedly higher fracturing pumping pressure. Meanwhile, the elevated formation pressure reduces fluid leak-off into the matrix, which significantly accelerates fracture propagation, as shown in Fig. 18(b).

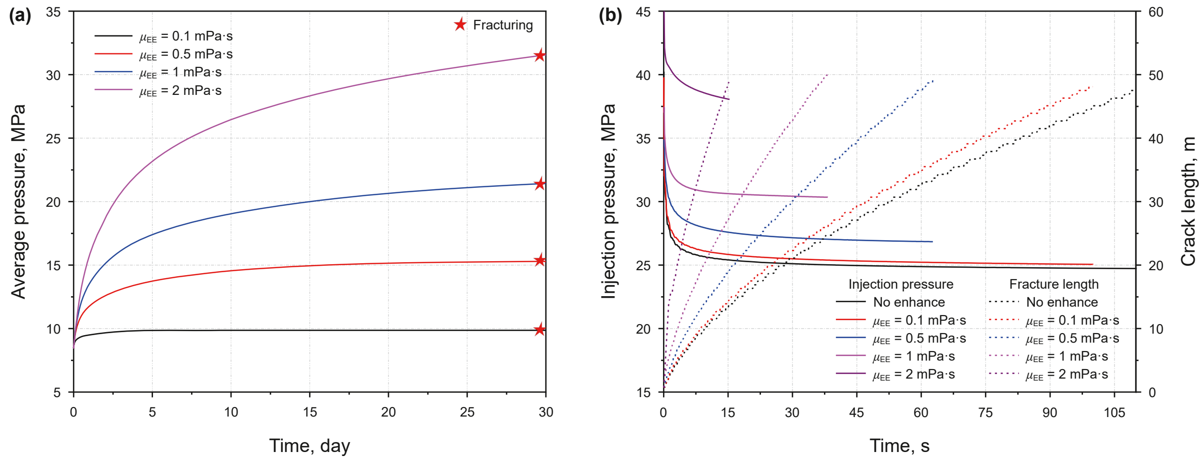

Fig. 18. Temporal evolution of key variables: (**a**) average pressure during EE; (**b**) injection pressure and fracture length during hydraulic fracturing.

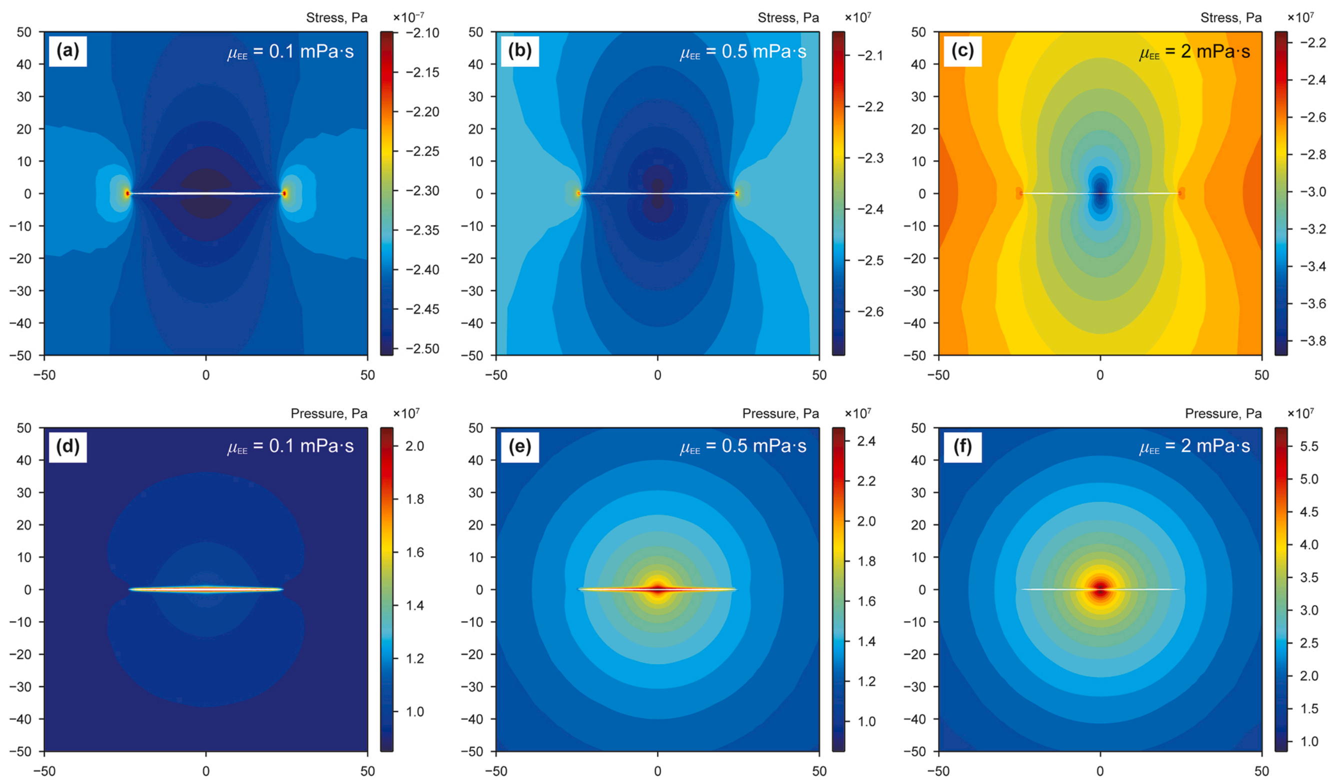

Fig. 19. Numerical results of stress and pressure when $L_{HF} = 50$ m: (**a**)–(**c**) minimum horizontal stress with $\mu_{EE} = 0.1$, 0.5, and 2 mPa·s; (**d**)–(**f**) pore pressure with $\mu_{EE} = 0.1$, 0.5, and 2 mPa·s.

Fig. 20 illustrates the impact of energy-enhanced fluid viscosity on the fracture aperture distribution after HFs propagate to a length of 50 m. With increasing μ_{EE}, the aperture profile of the HF changes from a classical elliptical shape to a saddle-shaped profile. This transformation is attributed to changes in the total minimum horizontal stress near the injection point. As a result, the maximum fracture aperture at the initiation point decreases markedly, from 1.5 mm in the case without EE to only 0.201 mm when the EE fluid viscosity reaches 2 mPa·s. Overall, the simulation results demonstrate that a higher EE fluid viscosity leads to more pronounced stress field modification due to EE, which significantly impacts subsequent fracture propagation.

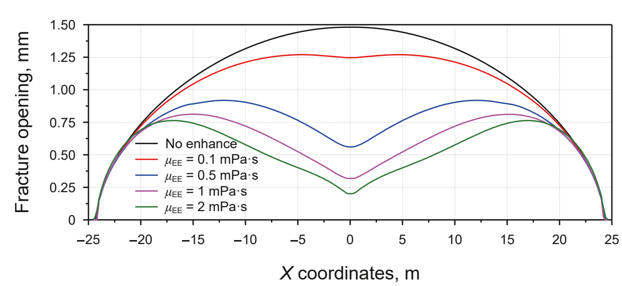

Fig. 20. Fracture aperture distributions for different μ_{EE} when $L_{HF} = 50$ m.

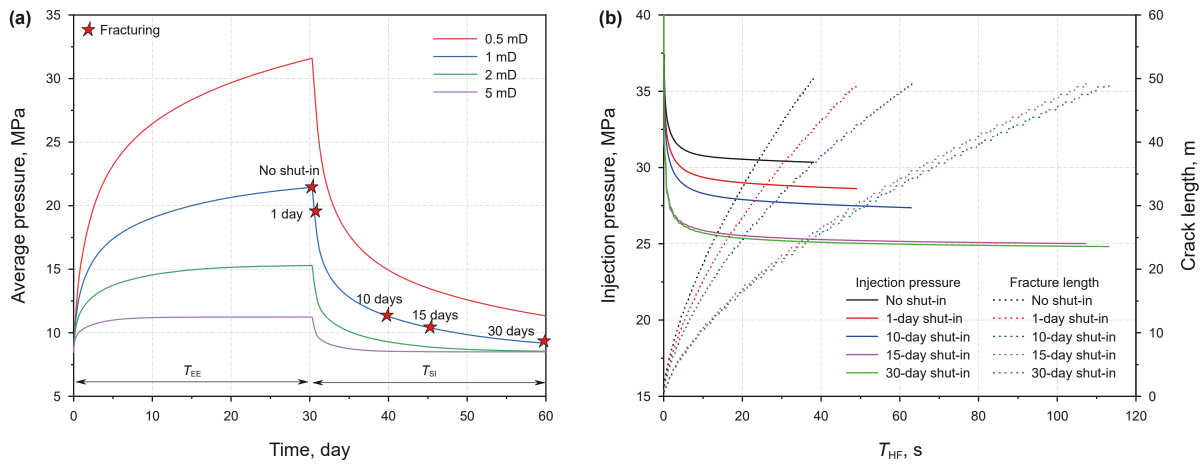

Fig. 21. Temporal evolution of key variables: (**a**) average pressure during EE; (**b**) injection pressure and fracture length during hydraulic fracturing.

4.2.6. Shut-in time after EE

This section investigates the influence of shut-in duration (T_{SI}) after energy-enhanced injection on subsequent hydraulic fracture propagation. Water is used as the energy-enhanced fluid, injected at a rate of $Q_{EE} = 3 \times 10^{-5}$ m^2/s per unit formation thickness into a formation with a permeability of 1 mD. Unlike previous cases, where hydraulic fracturing followed immediately after 30-day EE, the current simulations incorporate a shut-in period before hydraulic fracturing. Four shut-in durations are considered: 1, 10, 15, and 30 days. Hydraulic fracturing is initiated at the center of the model using the same operational parameters as in other sections. The input parameters are listed in Tables 4 and 5.

Fig. 21(a) shows the temporal evolution of the average formation pressure within a 25 m radius of the injection point during EE and shut-in stages for formations with different permeabilities. After shut-in begins, the formation pressure declines rapidly, with the rate of decline progressively decreasing over time. In the first 15 days of shut-in (T_{SI}: 0–15 days), the average pressure drops from 21.42 MPa to 10.43 MPa—a decrease of 10.99 MPa. In the subsequent 15 days (T_{SI}: 15–30 days), the pressure reduction slows considerably, amounting to only 1.26 MPa. This indicates that as T_{SI} increases, the energy-enhanced injected fluid progressively migrates away from the injection point, leading to continued dissipation of formation pressure. These pressure changes affect

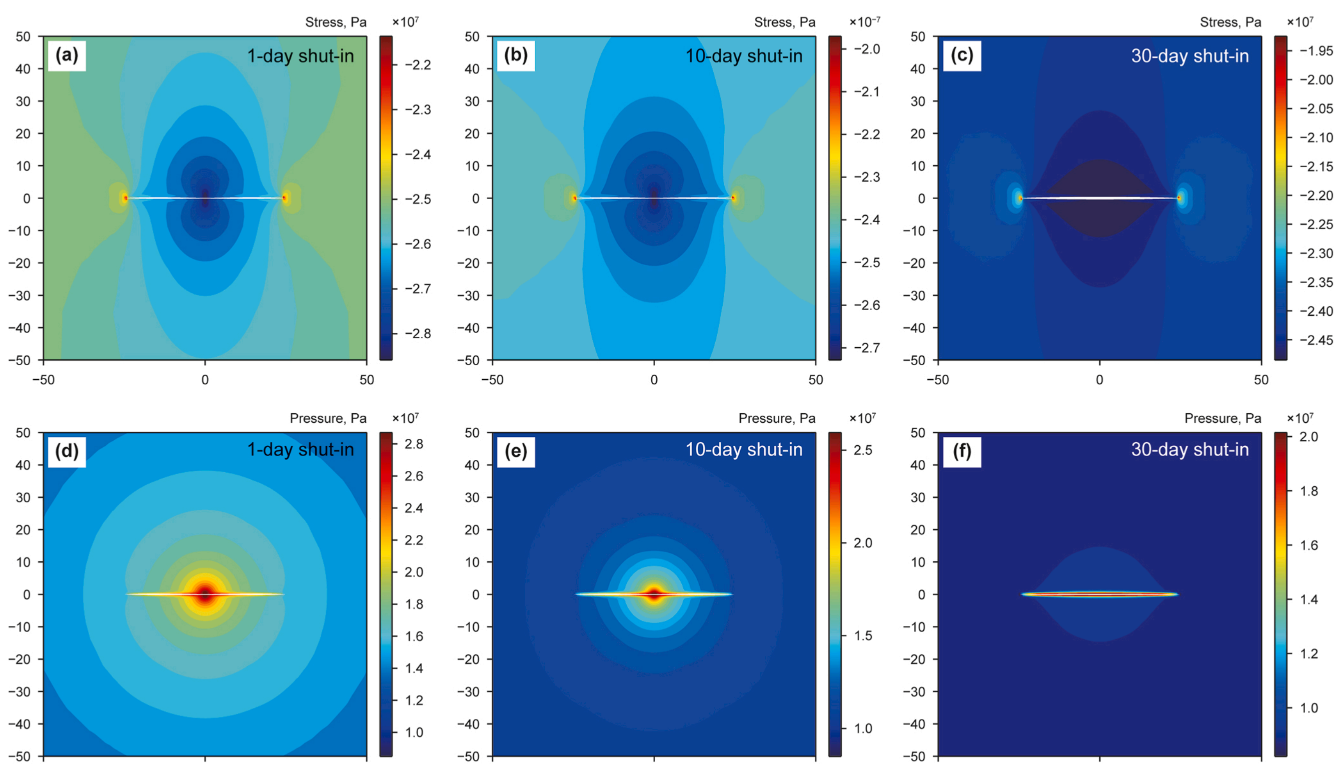

Fig. 22. Numerical results of stress and pressure when $L_{HF} = 50$ m: (**a**)–(**c**) minimum horizontal stress with $T_{SI} = 1$, 10, and 30 days; (**d**)–(**f**) pore pressure with $T_{SI} = 1$, 10, and 30 days.

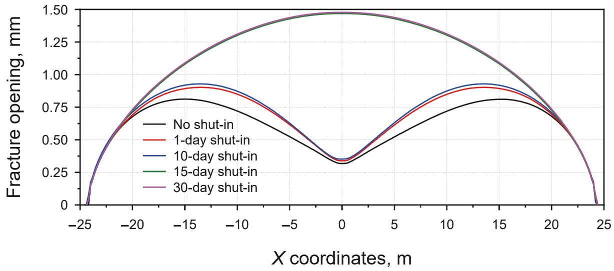

Fig. 23. Fracture aperture distributions for different T_{SI} when $L_{HF} = 50$ m.

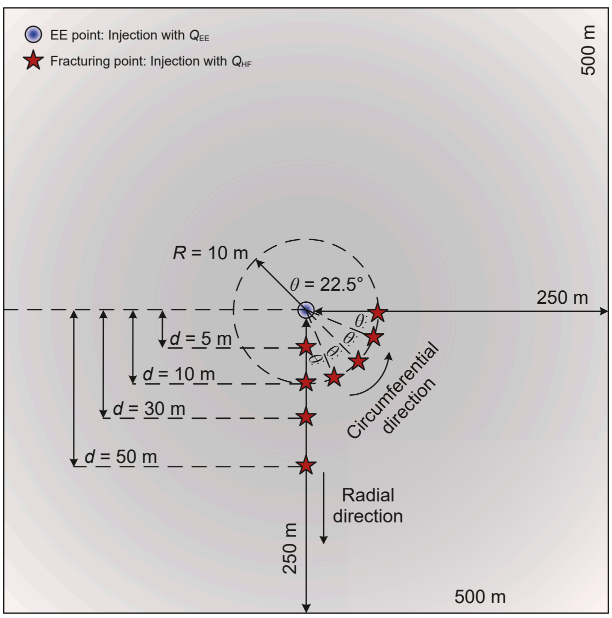

Fig. 24. Schematic of fracture initiation locations relative to the energy-enhanced injection point.

subsequent hydraulic fracture propagation, as shown in Fig. 21(b), which plots the evolution of injection pressure and fracture length. Extending the T_{SI} to 30 days reduces the fracture propagation pressure from 30.34 MPa to 24.82 MPa, closely matching the non-EE case (24.71 MPa). This reduction is primarily attributed to the drop in formation pressure, which leads to a corresponding decrease in minimum horizontal stress, as depicted in Fig. 22(a)–(c). A longer T_{SI} also noticeably slows fracture growth. For example, the fracture reaches 50 m in 38.22 s without shut-in but requires 113.19 s after a 30-day shut-in. Fig. 22(d)–(f) demonstrate that extended T_{SI} amplifies pore pressure dissipation, thereby increasing fluid leak-off and restricting fracture growth. Fig. 23 presents the fracture aperture distributions at a fracture length of 50 m for various T_{SI}. The results are consistent with previous analyses: shorter T_{SI} results in narrower apertures at the injection point, suggesting a stronger influence of the prior EE. Conversely, longer T_{SI} yields aperture distributions that resemble those of the non-EE case shown in Fig. 13, indicating that the influence of EE diminishes as T_{SI} increases.

4.2.7. Fracture initiation location after EE

This section investigates how the spatial offset between the fracturing point and the energy-enhanced point influences HF propagation, and quantifies the degree of deviation in fracture development. Water is used as the energy-enhanced fluid and injected at a rate of $Q_{EE} = 3 \times 10^{-5}$ m^2/s into a formation with a permeability of 1 mD. Hydraulic fracturing begins immediately after 30 days of energy-enhanced injection. Given the radial pressure distribution induced by the EE treatment, two scenarios are analyzed. The first investigates the influence of the radial distance between the energy-enhanced point and the fracturing point on the development of HF. The second examines how circumferential variation at a fixed radius impacts fracture propagation behavior. As shown in Fig. 24, the first scenario includes four fracturing points positioned at radial distances of 5, 10, 30, and 50 m from the EE point. The second scenario involves five points arranged circumferentially at a constant radius of 10 m, with azimuthal angles of 0°, 22.5°, 45°, 67.5°, and 90° relative to the vertical axis. All other input parameters and rock mechanical properties are held constant, as specified in Tables 4 and 5 These results provide insights into the influence of prior EE on fracture growth in adjacent wells or at different locations within the same well.

(a) Fracture initiation along radial direction

Fig. 25(a) presents the temporal evolution of injection pressure and fracture length during hydraulic fracturing initiated at different locations along the negative y-axis after EE at the origin (0, 0). As the distance (denoted as d) between the initiation point

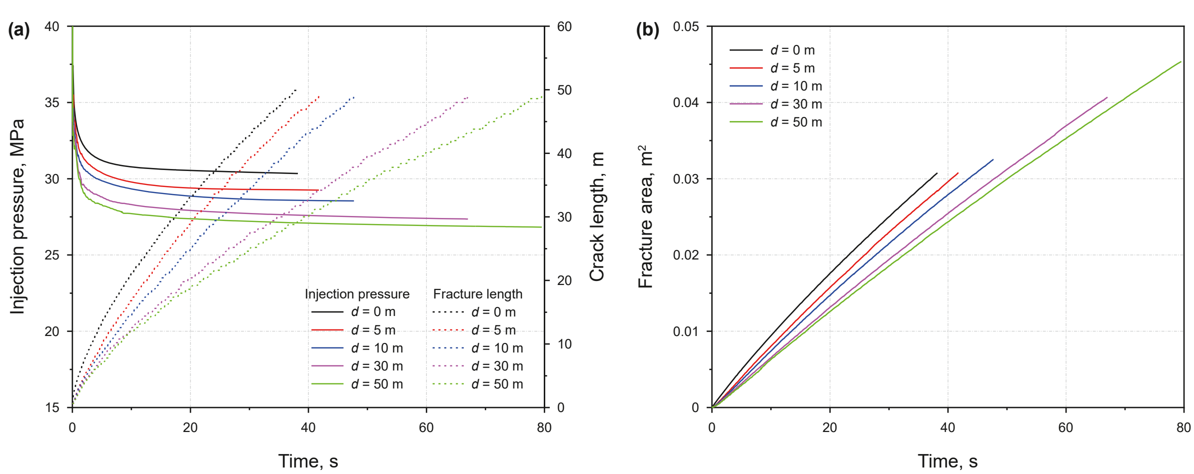

Fig. 25. Temporal evolution of HF propagation at different radial distance: (**a**) injection pressure and fracture length; (**b**) fracture area.

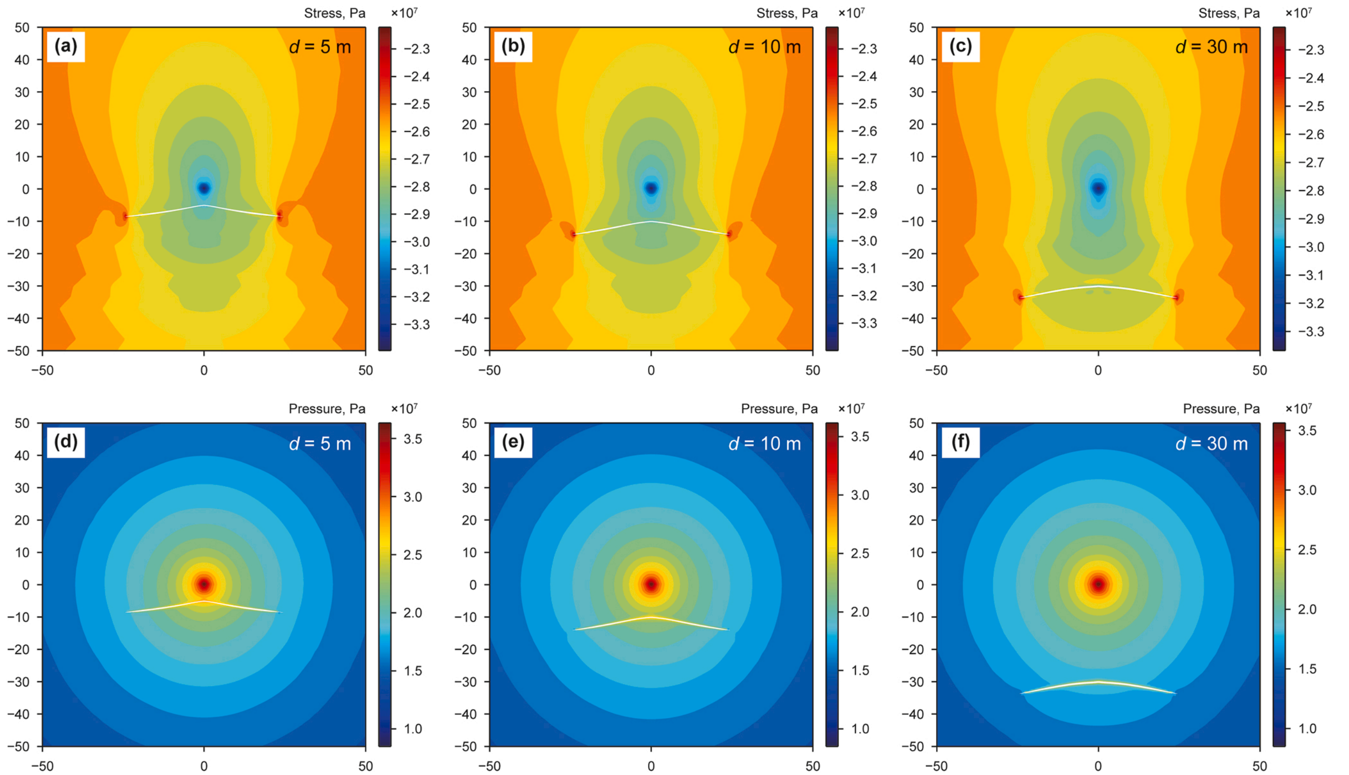

Fig. 26. Numerical results of stress and pressure when $L_{HF} = 50$ m: (**a**)–(**c**) minimum horizontal stress with $d = 5$, 10, and 30 m; (**d**)–(**f**) pore pressure with $d = 5$, 10, and 30 m.

and the energy-enhanced injection point increases, the injection pressure gradually declines. For example, the fracture propagation pressure drops from 30.34 MPa at $d = 0$ m to 26.83 MPa at $d = 50$ m. However, moving the initiation point outward also slows fracture growth: a fracture reaching 50 m takes 38 s when starting at the energy-enhanced point ($d = 0$ m) but almost twice as long (79.5 s) when starting 50 m away. Fig. 25(b) further illustrates this effect: at 38.2 s, the fracture area decreases from 0.03 m^2 to 0.0233 m^2 as the initiation point moves 50 m away from the energy-enhanced point. These trends are driven by changes in the stress and pressure magnitudes caused by the movement of the initiation points. As shown in Fig. 26(a)–(c), greater distances correspond to lower minimum horizontal principal stress, which reduces the propagation pressure required for HFs. At the same time, formation pressure also declines with increasing distance, as shown in Fig. 26(d)–(f), thereby increasing the pressure differential between the fracturing fluid and the formation. This leads to greater fluid leak-off and diminished fracturing efficiency.

In earlier analyses, the fracture was assumed to initiate at the same location as the energy-enhanced injection point. As discussed in Section 4.2.2, the principal stress directions near $y = 0$ remain unchanged, resulting in horizontal fracture growth identical to that under the original in-situ stress field. However, when the initiation point is radially moved along the negative y-axis, changes in stress direction cause the fractures to deviate (Fig. 26). Despite this deviation, the symmetry of the stress and pressure fields about the y-axis ensures symmetric fracture geometries. To compare how deviation varies with increasing d, all initiation points were translated to a common origin at (0, 0) in Fig. 27. The plots show that fractures initiated closer to the energy-enhanced point exhibit sharper initial deviations. For example, when the fracture length is less than 25 m, the greatest deviation is observed in the case of $d = 5$ m, where the fracture deflects nearly 2 m from the injection point. As propagation continues, the fracture gradually realigns with the horizontal direction. The maximum deflection occurs at $d = 10$ m, where the final tip displaces 3.96 m from the initiation point when $L_{HF} = 50$ m. This pattern is consistent with the stress rotation contours shown in Fig. 8. Along the negative y-axis, stress rotation decreases with increasing distance from the energy-enhanced point near $x = 0$. Fractures propagate along the direction of maximum principal stress, with stress rotation peaking at about 45° before diminishing. This explains

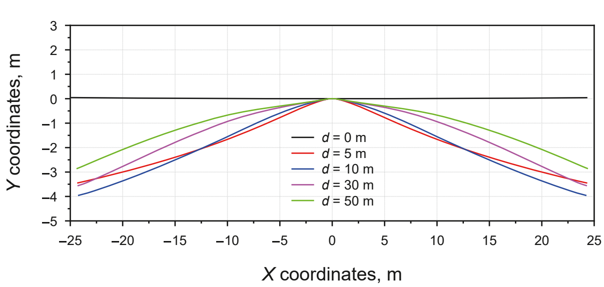

Fig. 27. Fracture propagation path for different radial distance when $L_{HF} = 50$ m.

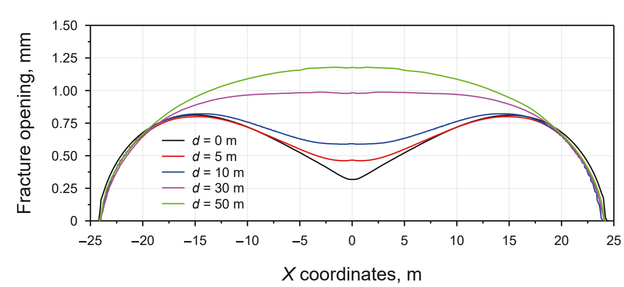

Fig. 28. Fracture aperture distributions for different radial distance when $L_{HF} = 50$ m.

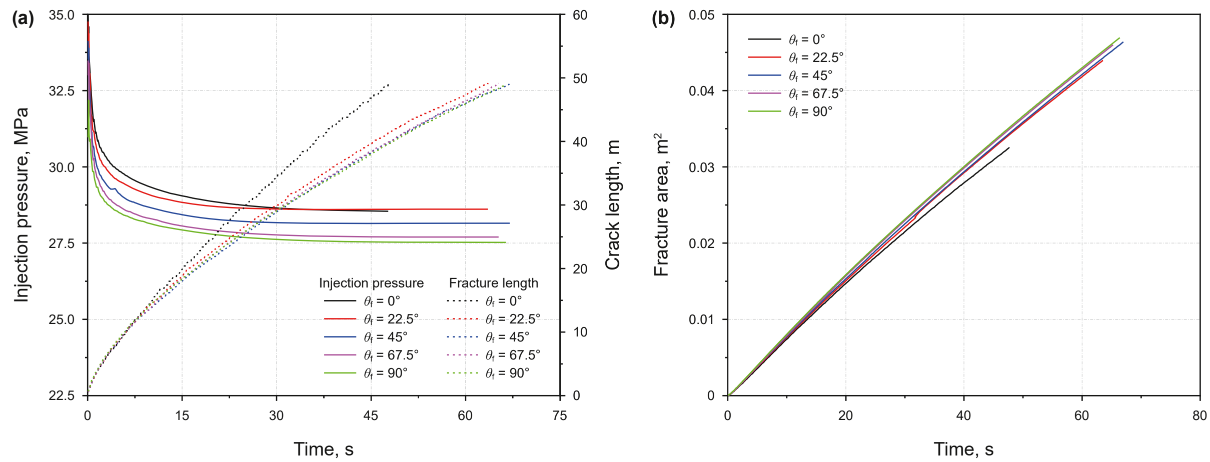

Fig. 29. Temporal evolution of HF propagation at different circumferential positions: (**a**) injection pressure and fracture length; (**b**) fracture area.

why the deflection of fractures initially increases and then decreases for $d = 5$, 10, and 30 m. Fig. 28 shows the distribution of fracture aperture. As d increases, the aperture near the injection point becomes larger. Beyond 30 m, the previously observed saddle-shaped aperture distribution disappears and transitions back to an elliptical form, indicating diminished influence of EE.

(b) Fracture initiation along circumferential direction

Fig. 29(a) shows the temporal evolution of injection pressure and fracture length during hydraulic fracturing, with the initiation point fixed 10 m from the energy-enhanced injection point but located at different circumferential positions. Here, θ_f denotes the angle between the line connecting the initiation and energy-enhanced injection points and the negative y-axis. As θ_f increases, the pressure required to propagate the fracture decreases. For example, when $\theta_f = 0°$ (along the negative y-axis), the propagation pressure is 28.55 MPa, while at $\theta_f = 90°$ (along the positive x-axis), it drops to 27.52 MPa. Despite this pressure variation, Fig. 29(b) shows that the overall fracture growth rate and fracturing efficiency remain similar across most cases, except for $\theta_f = 0°$. This behavior can be attributed to the asymmetric stress and pore pressure distributions shown in Fig. 30. Once initiation points deviate from the negative y-axis, the surrounding stress field becomes asymmetric, favoring rightward fracture propagation due to lower stress on the right side. As shown in Fig. 30, the minimum principal stress at the initiation point decreases as θ_f increases, which is the main reason for the reduction in injection pressure. To facilitate comparison of fracture deflection under

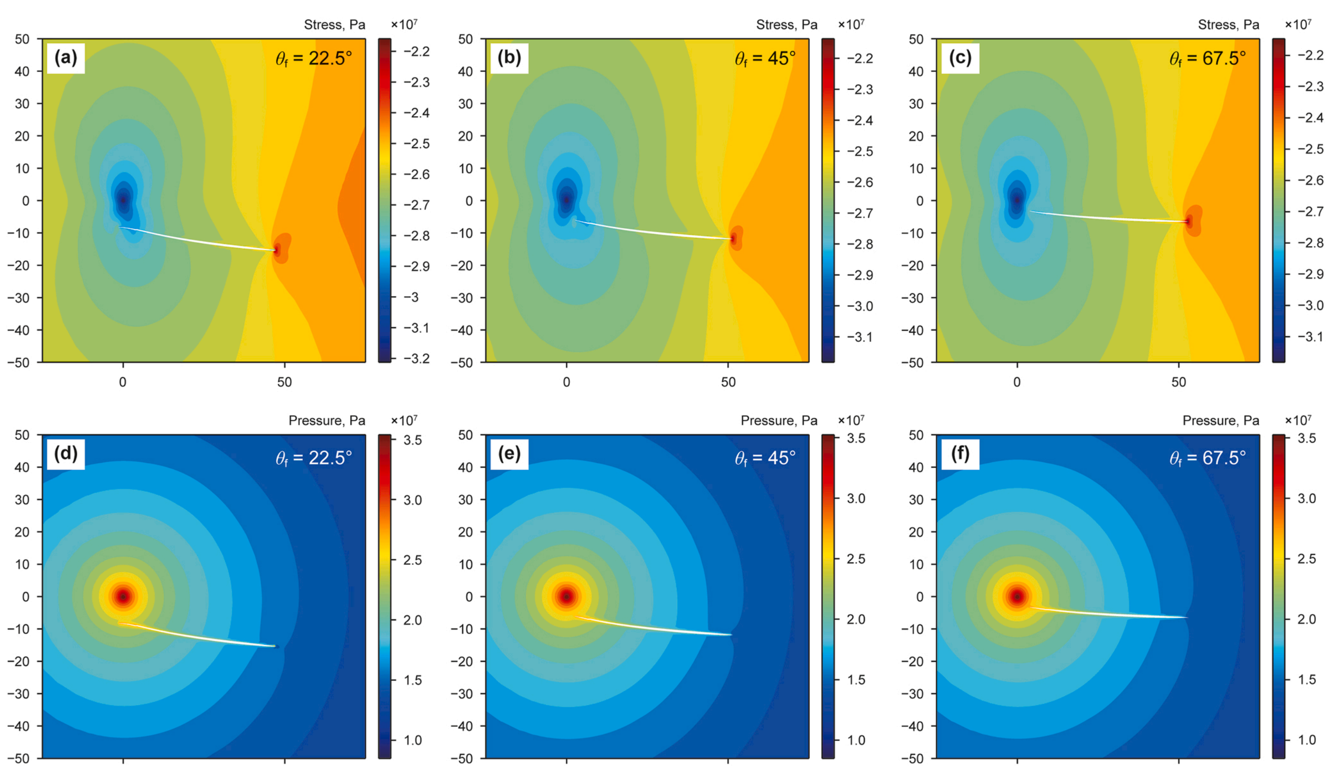

Fig. 30. Numerical results of stress and pressure when $L_{HF} = 50$ m: (**a**)–(**c**) minimum horizontal stress with $\theta_f = 22.5°$, 45°, 67.5°; (**d**)–(**f**) pore pressure with $\theta_f = 22.5°$, 45°, 67.5°.

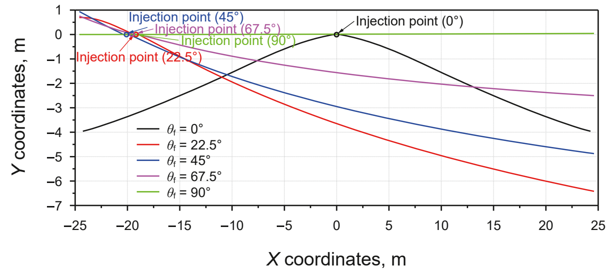

Fig. 31. Fracture propagation path at different circumferential positions when $L_{HF} = 50$ m.

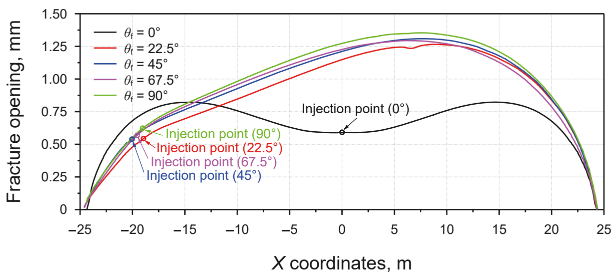

Fig. 32. Fracture aperture distributions at different circumferential positions when $L_{HF} = 50$ m.

different conditions, all initiation points were translated along the x-axis, as shown in Fig. 31. The results indicate that fracture deflection decreases as θ_f increases. The vertical offset along the y-axis drops from 6.4 m at $\theta_f = 22.5°$ to 2.5 m at $\theta_f = 67.5°$, largely because the $\theta_f = 22.5°$ fracture lies within the zone of larger stress rotation caused by EE (Fig. 8(e)). Fig. 32 shows that, except for $\theta_f = 0°$, the fracture aperture distributions are generally consistent across different cases. However, when $\theta_f > 0°$, the lower stress on the right favors rightward growth, resulting in longer fractures and wider apertures. When the total fracture length reaches 50 m, the maximum aperture occurs approximately 15 m from the right tip.

Overall, when initiation points deviate from the y-axis, asymmetric fracture propagation is observed. Although the aperture distribution remains similar, fractures initiated closer to the y-axis tend to exhibit greater deflection. Among all numerical cases, the $\theta_f = 90°$ case yields the lowest injection pressure, the highest propagation efficiency, and the simplest fracture geometry, thereby contributing to proppant transport.

5. Discussion

This study employs a fully coupled XFEM model to investigate how EE influences subsequent hydraulic fracturing. The analysis focuses on the roles of reservoir properties (matrix permeability), EE operational parameters (injection volume, injection rate, fluid viscosity, and shut-in time), and fracture initiation location in controlling the geometry and evolution of HFs. The simulation results show that EE injection substantially elevates pore pressure and total confining stress near the injection well, and also alters the local stress orientation. These EE-induced changes in stress and pore pressure strongly govern the behavior of subsequent fracture growth. First, EE injection increases the minimum horizontal stress in the reservoir, which raises the pressure required to initiate and propagate fractures and may increase operational risk. Second, the accompanying rise in pore pressure reduces fluid loss to the formation and promotes faster fracture extension. Furthermore, the parametric sensitivity analysis indicates that lower reservoir permeability, larger EE injection volume, higher injection rate, and higher EE fluid viscosity result in slower dissipation of pore pressure after EE injection. Consequently, the impact of the EE process on subsequent hydraulic fracturing becomes more pronounced. In addition, the results highlight the importance of fracture initiation location within the EE-affected zone, as different initiation locations lead to distinctly different fracture morphologies. The high-stress region created by EE injection functions as a stress barrier, which limits fracture opening and deflects fracture paths away from the EE injection zone. The mechanisms identified in this study provide practical insight for optimizing integrated EE-fracturing designs.

To clearly elucidate the core mechanism of how pre-fracturing EE alters the near-wellbore stress field and influences subsequent HF propagation, this study adopted several simplifying assumptions for a clearer and more computationally efficient analysis. Firstly, the reservoir was assumed to be a homogeneous porous medium, without considering non-homogeneities such as natural fractures or bedding planes. Secondly, the model employed a 2D planar fracture with a constant height based on the KGD model, which inherently limits its ability to simulate 3D vertical growth or interaction with multiple layers. Thirdly, both the energy-enhanced fluid and the fracturing fluid were treated as Newtonian fluids, without considering the shear-rate dependence of fracturing fluid viscosity. We acknowledge that these simplifications constitute the primary limitations of the current model, as factors like formation heterogeneity, 3D vertical fracture growth, and the non-Newtonian flow behavior of fracturing fluids can significantly influence HF propagation (Zhang et al., 2024; Wrobel et al., 2021; Sun et al., 2025). Consequently, future work will focus on developing a more comprehensive, fully coupled 3D model to investigate the effects of geological heterogeneity and non-Newtonian fluid rheology on the HF propagation following EE.

6. Conclusions

This study investigates the influence of pre-fracturing EE on HF propagation using a fully coupled XFEM model. The main conclusions can be summarized as follows.

(1) Pre-fracturing EE injection exerts two competing effects on hydraulic fracturing. EE can improve fracturing efficiency (e.g., from 51.09% to 80.5% in a 1 mD formation) by reducing fluid leak-off due to elevated pore pressure. At the same time, EE injection raises the confining stress and hence increases the injection pressure (by over 5.63 MPa under the same conditions), thereby increasing pumping risk.

(2) Low-permeability formations (e.g., <1 mD) experience the most significant stress alteration and pressure buildup, making hydraulic fracturing in these formations highly sensitive to EE. The effect diminishes as permeability increases and becomes negligible above approximately 5 mD for the studied parameters.

(3) Larger injection volumes, higher injection rates and fluid viscosity, and shorter shut-in times all strengthen the influence of EE on subsequent HF propagation.

(4) The high-stress region created by EE injection functions as a stress barrier, which limits fracture opening and deflects fracture paths away from the EE injection zone. A radial offset along the initial minimum stress direction causes fracture deflection, with a 10 m offset reaching the maximum deviation at 3.96 m for the studied parameters.

(5) Hydraulic fracturing near an energy-enhanced injection well is prone to pronounced asymmetric propagation: the

fracture wing closer to the energy-enhanced injection point curves toward it and experiences growth suppression, while the opposing wing propagates preferentially.

CRediT authorship contribution statement

Pin-Jin Zhang: Writing – original draft. **Yun Zhou:** Writing – review & editing, Software, Methodology. **Shan-Po Jia:** Visualization, Validation, Supervision. **Zong-Feng Zhang:** Visualization, Investigation. **Bin-Tao Wang:** Data curation. **Dian-Sen Yang:** Project administration, Funding acquisition, Formal analysis.

Data availability

Data will be made available on request.

Declaration of competing interest

The authors declare that they have no known competing financial interests or personal relationships that could have appeared to influence the work reported in this paper.

Acknowledgements

This work was supported by Hebei Natural Science Foundation (Grant No. E2025107007), Heilongjiang Provincial Natural Science Foundation of China (Grant No. YQ2025E006), National Natural Science Foundation of China (Grant Nos. 12202463, U22A20595, 42293353), Natural Science Foundation of Hubei Province (Grant No. 2024AFA072), and Youth Innovation Promotion Association CAS (Grant No. 2022332).

References

Adachi, J.I., Detournay, E., 2008. Plane strain propagation of a hydraulic fracture in a permeable rock. Eng. Fract. Mech. 75 (16), 4666–4694. https://doi.org/10.1016/j.engfracmech.2008.04.006.

AlTammar, M.J., Sharma, M.M., Manchanda, R., 2018. The effect of pore pressure on hydraulic fracture growth: an experimental study. Rock Mech. Rock Eng. 51 (9), 2709–2732. https://doi.org/10.1007/s00603-018-1500-7.

Atefi-Monfared, K., Rybicki, J., 2018. Production versus injection induced poroelasticity surrounding wells. J. Petrol. Sci. Eng. 162, 102–113. https://doi.org/10.1016/j.petrol.2017.12.025.

Belytschko, T., Black, T., 1999. Elastic crack growth in finite elements with minimal remeshing. Int. J. Numer. Methods Eng. 45 (5), 601–620. https://doi.org/10.1002/(sici)1097-0207(19990620)45:5<601::aid-nme598>3.0.co;2-s.

Carrier, B., Granet, S., 2012. Numerical modeling of hydraulic fracture problem in permeable medium using cohesive zone model. Eng. Fract. Mech. 79, 312–328. https://doi.org/10.1016/j.engfracmech.2011.11.012.

Deng, Y., Mu, S., Liu, Y., et al., 2024. Numerical simulation of stress field reorientation in multi-fractures. Geomech. Geophys. Geo Energy Geo Resour. 10 (1), 36. https://doi.org/10.1007/s40948-024-00745-1.

Detournay, E., Cheng, A.H., 1988. Poroelastic response of a borehole in a non-hydrostatic stress field. Int. J. Rock Mech. Min. Sci. Geomech. Abstr. 25 (3), 171–182. https://doi.org/10.1016/0148-9062(88)92299-1.

Detournay, E., 2004. Propagation regimes of fluid-driven fractures in impermeable rocks. Int. J. GeoMech. 4 (1), 35–45. https://doi.org/10.1061/(asce)1532-3641(2004)4:1(35.

Dong, J., Qu, H., Zhang, J., et al., 2023. Numerical simulation of hydraulic fracture propagation under energy supplement conditions. Front. Earth Sci. 11, 1269159. https://doi.org/10.3389/feart.2023.1269159.

Erdogan, F., Sih, G.C., 1963. On the crack extension in plates under plane loading and transverse shear. J. Basic Eng. 85 (4), 519–525. https://doi.org/10.1115/1.3656897.

Gao, Q., Cheng, Y., Han, S., et al., 2019. Numerical modeling of hydraulic fracture propagation behaviors influenced by pre-existing injection and production wells. J. Petrol. Sci. Eng. 172, 976–987. https://doi.org/10.1016/j.petrol.2018.09.005.

Guo, X., Wu, K., An, C., et al., 2019. Numerical investigation of effects of subsequent parent-well injection on interwell fracturing interference using reservoir-geomechanics-fracturing modeling. SPE J. 24 (4), 1884–1902. https://doi.org/10.2118/195580-pa.

Gupta, J.K., Zielonka, M.G., Albert, R.A., et al., 2012. Integrated methodology for optimizing development of unconventional gas resources. In: SPE Hydraulic Fracturing Technology Conference, Richardson. Society of Petroleum Engineers, pp. SPE 152224–MS. https://doi.org/10.2118/152224-ms.

Hu, J., Garagash, D.I., 2010. Plane-strain propagation of a fluid-driven crack in a permeable rock with fracture toughness. J. Eng. Mech. 136 (9), 1152–1166. https://doi.org/10.1061/(asce)em.1943-7889.0000169.

Hu, S., Wei, C., Yan, Y., et al., 2024. Study on the pattern of hydraulic fracture propagation andfracture conductivity of conglomerate with different lithologiesin Ma'nan area. Comput. Energy Sci. 1 (2), 69–85. https://doi.org/10.46690/compes.2024.02.02.

Ji, B., Fang, J., 2023. An overview of efficient development practices at low permeability sandstone reservoirs in China. Energy Geosci 4 (3), 100179. https://doi.org/10.1016/j.engeos.2023.100179.

Khoei, A.R., 2014. Extended Finite Element Method: Theory and Applications. John Wiley & Sons, Chichester. https://doi.org/10.1002/9781118869673.

Li, X., Wang, J., Elsworth, D., 2017. Stress redistribution and fracture propagation during restimulation of gas shale reservoirs. J. Petrol. Sci. Eng. 154, 150–160. https://doi.org/10.1016/j.petrol.2017.04.027.

Li, X., 2024. Fracture reorientation mechanism during hydraulic fracturing based on XFEM simulation. Front. Earth Sci. 12, 1503934. https://doi.org/10.3389/feart.2024.1503934.

Li, Y., Yang, H., Li, B., et al., 2025. Interference behaviour between bedding planes and hydraulic fractures and its influence on the complex fracture network in shale. Rock Mech. Rock Eng. 58 (1), 181–201. https://doi.org/10.1007/s00603-024-04167-z.

Lu, M., Su, Y., Gutierrez, M., et al., 2020. Verification of fracture reorientation and analysis of influence factors in multiple fracturing treatment. Geofluids 2020, 2457814. https://doi.org/10.1155/2020/2457814.

Ma, W., Wu, K., Jin, G., 2024. Investigation of effective fracture height using strain responses in a vertical monitoring well during a well interference test. In: SPE Hydraulic Fracturing Technology Conference and Exhibition, Richardson. Society of Petroleum Engineers, p. SPE 217776. https://doi.org/10.2118/217776-ms. MS.

Ma, W., Wu, K., Jin, G., 2023. Geomechanics modeling of strain-based pressure estimates: insights from distributed fiber optic strain measurements. In: Proceedings of the 11th Unconventional Resources Technology Conference. American Association of Petroleum Geologists. https://doi.org/10.15530/urtec-2023-3864861.

Melenk, J.M., Babuška, I., 1996. The partition of unity finite element method: basic theory and applications. Comput. Methods Appl. Mech. Eng. 139 (1–4), 289–314. https://doi.org/10.1016/S0045-7825(96)01087-0.

Moës, N., Belytschko, T., 2002. Extended finite element method for cohesive crack growth. Eng. Fract. Mech. 69 (7), 813–833. https://doi.org/10.1016/S0013-7944(01)00128-X.

Moës, N., Cloirec, M., Cartraud, P., et al., 2003. A computational approach to handle complex microstructure geometries. Comput. Methods Appl. Mech. Eng. 192 (28–30), 3163–3177. https://doi.org/10.1016/S0045-7825(03)00346-3.

Moës, N., Dolbow, J., Belytschko, T., 1999. A finite element method for crack growth without remeshing. Int. J. Numer. Methods Eng. 46 (1), 131–150. https://doi.org/10.1002/(sici)1097-0207(19990910)46:1<131::aid-nme726>3.0.co;2-j.

Paris, P.C., Sih, G.C., 1965. Stress analysis of cracks. In: Fracture Toughness Testing and its Applications, ASTM International100 Barr Harbor Drive. PO Box C700, West Conshohocken, PA, pp. 30–81. https://doi.org/10.1520/stp26584s, 19428-2959.

Paul, B., Faivre, M., Massin, P., et al., 2018. 3D coupled HM–XFEM modeling with cohesive zone model and applications to non planar hydraulic fracture propagation and multiple hydraulic fractures interference. Comput. Methods Appl. Mech. Eng. 342, 321–353. https://doi.org/10.1016/j.cma.2018.08.009.

Réthoré, J., de Borst, R., Abellan, M.A., 2007. A two-scale approach for fluid flow in fractured porous media. Int. J. Numer. Methods Eng. 71 (7), 780–800. https://doi.org/10.1002/nme.1962.

Safari, R., Lewis, R., Ma, X., et al., 2017. Infill-well fracturing optimization in tightly spaced horizontal wells. SPE J. 22 (2), 582–595. https://doi.org/10.2118/178513-pa.

Shi, X., Ge, X., Gao, Q., et al., 2024. Numerical simulation of hydraulic fracture propagation from recompletion in refracturing with dynamic stress modeling. Geomech. Geophys. Geo Energy Geo Resour. 10 (1), 155. https://doi.org/10.1007/s40948-024-00880-9.

Siebrits, E., Elbel, J.L., Hoover, R.S., et al., 2000. Refracture reorientation enhances gas production in Barnett Shale tight gas wells. In: SPE Annual Technical Conference and Exhibition, Richardson. Society of Petroleum Engineers, p. SPE 63030. https://doi.org/10.2118/63030-ms. MS.

Sun, D., Xu, F., Ma, L., et al., 2025. Mechanism of hydraulic fracture propagation and fracturing process optimization in thin-interbedded sandstone-shale reservoirs based on 3D discrete lattice method. Front. Earth Sci. 13, 1602646. https://doi.org/10.3389/feart.2025.1602646.

Wang, S.Y., Sloan, S.W., Fityus, S.G., et al., 2013. Numerical modeling of pore pressure influence on fracture evolution in brittle heterogeneous rocks. Rock Mech. Rock Eng. 46 (5), 1165–1182. https://doi.org/10.1007/s00603-012-0330-2.

Wang, X.H., Zhang, F.S., Yin, Z.R., et al., 2022. Numerical investigation of refracturing with/without temporarily plugging diverters in tight reservoirs. Pet. Sci. 19 (5), 2210–2226. https://doi.org/10.1016/j.petsci.2022.05.006.
Wang, Q., Zhao, J., Hu, Y., et al., 2024. Optimization method of refracturing timing for old shale gas wells. Petrol. Explor. Dev. 51 (1), 213–222. https://doi.org/10.1016/S1876-3804(24)60018-2.
Wang, Q., Wang, Y., Wang, R., et al., 2025. Evolution law of stress induced by pressure depletion in fractured shale reservoirs: Implications for subsequent refracturing and infill well development. Petroleum 11 (1), 71–83. https://doi.org/10.1016/j.petlm.2024.04.001.
Wei, Z., Sheng, M., Li, J., et al., 2025. Pressure diagnostics in hydraulic fracturing for unconventional completion optimization. Adv. Geo-Energy Res. 17 (3), 196–211. https://doi.org/10.46690/ager.2025.09.03.
Witherspoon, P.A., Wang, J.S.Y., Iwai, K., et al., 1980. Validity of cubic law for fluid flow in a deformable rock fracture. Water Resour. Res. 16 (6), 1016–1024. https://doi.org/10.1029/wr016i006p01016.
Wrobel, M., Mishuris, G., Papanastasiou, P., 2021. On the influence of fluid rheology on hydraulic fracture. Int. J. Eng. Sci. 158, 103426. https://doi.org/10.1016/j.ijengsci.2020.103426.
You, S., Liao, Q., Yue, Y., et al., 2025. Enhancing fracture geometry monitoring in hydraulic fracturing using radial basis functions and distributed acoustic sensing. Adv. Geo-Energy Res. 16 (3), 260–275. https://doi.org/10.46690/ager.2025.06.06.
Yuan, B., Wood, D.A., Yu, W., 2015. Stimulation and hydraulic fracturing technology in natural gas reservoirs: theory and case studies (2012–2015). J. Nat. Gas Sci. Eng. 26, 1414–1421. https://doi.org/10.1016/j.jngse.2015.09.001.
Zhang, F.S., Huang, L.K., Yang, L., et al., 2022. Numerical investigation on the effect of depletion-induced stress reorientation on infill well hydraulic fracture propagation. Pet. Sci. 19 (1), 296–308. https://doi.org/10.1016/j.petsci.2021.09.014.
Zhang, Y., Guo, T., Chen, M., et al., 2024. Numerical simulation study of fracture height growth considering the influence of bedding planes. Comput. Geotech. 168, 106144. https://doi.org/10.1016/j.compgeo.2024.106144.
Zhou, L., Gou, Y., Hou, Z., et al., 2015. Numerical modeling and investigation of fracture propagation with arbitrary orientation through fluid injection in tight gas reservoirs with combined XFEM and FVM. Environ. Earth Sci. 73 (10), 5801–5813. https://doi.org/10.1007/s12665-015-4051-1.
Zhou, Y., Yang, D., Zhang, X., et al., 2020. Numerical investigation of the interaction between hydraulic fractures and natural fractures in porous media based on an enriched FEM. Eng. Fract. Mech. 235, 107175. https://doi.org/10.1016/j.engfracmech.2020.107175.
Zhu, H.Y., Song, Y.J., Tang, X.H., 2021. Research progress on 4-dimensional stress evolution and complex fracture propagation of infill wells in shale gas reservoirs. Pet. Sci. Bull. 6 (3), 396–416. https://doi.org/10.3969/j.issn.2096-1693.2021.03.032 (in Chinese).
Zienkiewicz, O.C., Chan, A.H.C., Pastor, M., et al., 1999. Computational Geomechanics with Special Reference to Earthquake Engineering. John Wiley & Sons, New York.